

Time-dependent nuclear energy-density functional theory toolkit for neutron star crust: dynamics of a nucleus in a neutron superfluid

Daniel Peçak,^{1,2,*} Agata Zdanowicz,¹ Nicolas Chamel,^{3,†} Piotr Magierski,^{1,4,‡} and Gabriel Wlazłowski^{1,4,§}

¹*Faculty of Physics, Warsaw University of Technology, Ulica Koszykowa 75, 00-662 Warsaw, Poland*

²*Institute of Physics, Polish Academy of Sciences, Aleja Lotników 32/46, PL-02668 Warsaw, Poland*

³*Institut d'Astronomie et d'Astrophysique, CP-226, Université Libre de Bruxelles, 1050 Brussels, Belgium*

⁴*Department of Physics, University of Washington, Seattle, WA 981951560, USA*

(Dated: March 27, 2024)

We present a new numerical tool designed to probe the dense layers of neutron star crusts. It is based on the Time-Dependent Hartree-Fock-Bogoliubov theory with generalized Skyrme nuclear energy density functionals, such as the Brussels-Montreal ones. We use it to study the time evolution of a nucleus accelerating through superfluid neutron medium in the inner crust of a neutron star. We extract an effective mass in the low velocity limit. We observe a threshold velocity and specify mechanisms of dissipation: phonon emission, Cooper pairs breaking, and vortex rings creation. The microscopic effects we study have impact on neutron star. Moreover, the mechanisms, we described, are general and apply also to other fermionic superfluid mixtures like liquid helium, or ultracold gases.

I. INTRODUCTION

Neutron stars are the compact remnants formed in the furnace of supernova explosions from the gravitational collapse of the core of progenitor stars with a zero-age main sequence mass $9 \lesssim M \lesssim 15M_{\odot}$ [1]. Initially very hot with temperatures reaching $\sim 10^{12}$ K, they rapidly cool down to $\sim 10^9$ K within days by releasing most of their energy in neutrinos (see, e.g., Refs. [2, 3]). The interior of a neutron star is so dense that it is highly degenerate and is expected to undergo various quantum phase transitions, as observed in some terrestrial materials at low-enough temperatures. In particular, neutrons present in the inner crust and in the core of a neutron star are thought to become superfluid by forming 1S_0 Cooper pairs, as in conventional superconductors. Although the existence of neutron superfluidity in neutron stars was predicted long ago before the actual discovery of these stars [4] and is now well-established, little is known about the properties of such nuclear condensates (see, e.g., Refs. [5, 6]). The conditions prevailing inside a neutron star are so extreme that they cannot be reproduced in the laboratory. The properties of their dense matter can be probed indirectly through astrophysical observations. However, microscopic models of cold dense matter remain crucial for constructing global models of superfluid neutron stars [7].

The most successful fully self-consistent approach for modeling quantum systems is via the Density Functional Theory (DFT). It has become a standard theoretical tool in electronic systems, delivering high-accuracy predictions while keeping the numerical cost at a reasonable

level, being of the same order as that of a mean-field method. In nuclear systems, the accuracy is still lower, but constant improvement of the quality of nuclear energy density functionals makes DFT¹ one of the leading approaches for describing the properties of nuclei across the whole nuclear chart, and beyond including nuclear matter under extreme astrophysical conditions (see review papers [11–14]). At the same time, the DFT is very flexible. There are a variety of extensions of the formalism: for static and time-dependent problems [15–17], zero and finite temperature problems [18–20], and for systems in normal and superconducting/superfluid states [21–26]. Implementing the DFT concept in the form of ready-to-use packages made it a workhorse for condensed-matter physics and quantum chemistry [27].

In this work, we provide a tool for numerical explorations of dense-matter properties under conditions expected to be found inside the inner crust of neutron stars. The tool exploits opportunities offered by DFT. Our method relies on recent nuclear energy density functional (EDF) developments. Specifically, we use a family of Brussels-Montreal Skyrme (BSk) nuclear functionals that have been optimized for astrophysical applications [28]. These functionals provide a high-quality global description of various properties of finite nuclei (masses, radii, ...) as well as properties of infinite nuclear matter in agreement with *ab-initio* calculations. We combine them with techniques of High-Performance Computing (HPC) that recently reached an enormous scale, being able to perform the order of 10^{18} mathematical operations per second. As a result, we construct a general-purpose toolkit for 3D modeling of dynamical processes that take place inside neutron stars. The toolkit that

* daniel.pecak@pw.edu.pl

† nicolas.chamel@ulb.be

‡ piotrm@uw.edu

§ gabriel.wlazlowski@pw.edu.pl

¹ Although we refer here to the DFT for both electronic and nuclear systems, some conceptual differences exist due to the breaking of symmetries in the latter [8–10].

hereafter we call W-BSk Toolkit [29], can deal with static and time-dependent phenomena at zero and finite temperatures without any symmetry constraints. The present HPC capabilities allow us to use it for modeling nuclear phenomena taking place in volumes exceeding $(100 \text{ fm})^3$ — volumes that are sufficient to encapsulate hundreds of thousands of neutrons and protons. For example, one of the relevant scales when studying neutron star crust is the radius of the spherical Wigner-Seitz (WS) cell. Its precise value depends on the depth in the crust, and microscopic calculations yield values in the range $R_{WS} \in (10 - 60) \text{ fm}$ [30]. The associated volumes of WS cell, $\frac{4}{3}\pi R_{WS}^3$, are within the reach of the toolkit; thus nowadays, phenomena taking place on the scales of WS cells can be simulated by means of the microscopic self-consistent DFT approach. Unlike electronic systems, superfluidity is crucial for describing nuclear systems. Indeed, the interactions between nucleons of the same species are naturally attractive at the densities of interest here, and the formation of Cooper pairs is therefore unavoidable. The standard way of taking into account superfluid properties requires the usage of nonlocal order parameter [21, 31]. Such an approach prevents its practical applications due to enormous numerical complexity. However, this was circumvented by formulating the problem using local pairing field [32] and the suitable framework had been developed (see review papers [13, 33, 34] and references therein). In this way, constructing an effective model of neutron star crust rooted in unified macroscopic formalism becomes feasible. In this paper we demonstrate this feasibility examining comprehensively the dynamical properties of a nucleus accelerating to the right through a nuclear cluster, called hereafter impurity, immersed in a neutron superfluid bath at zero temperature. Such configurations are expected to be present in neutron star crust, see Fig. 1.

In Sec. II we present the general theoretical framework, subsequently in Sec. III we elaborate on the physical problem where the framework can be applied. Next, in Sec. IV, we describe the numerical experiment tailored to tackle the physical problem. The results are presented in Sec. V (effective mass), and Sec. VI (dissipation channels). We conclude in Sec VII.

II. DFT AS GENERAL PURPOSE FRAMEWORK FOR NUCLEAR MATTER

The popularity of DFT methods arises from a very good balance of the quality of predictions to the computation cost. To avoid prohibitive computing times, we only consider semi-local functionals, such as the Brussels-Montreal BSk functionals [28]. These functionals, which were specifically constructed for astrophysical applications, are based on generalized Skyrme effective interactions with density-dependent t_1 and t_2 terms [36] together with microscopically deduced contact pairing interaction [37–39]. The resulting partial differential equa-

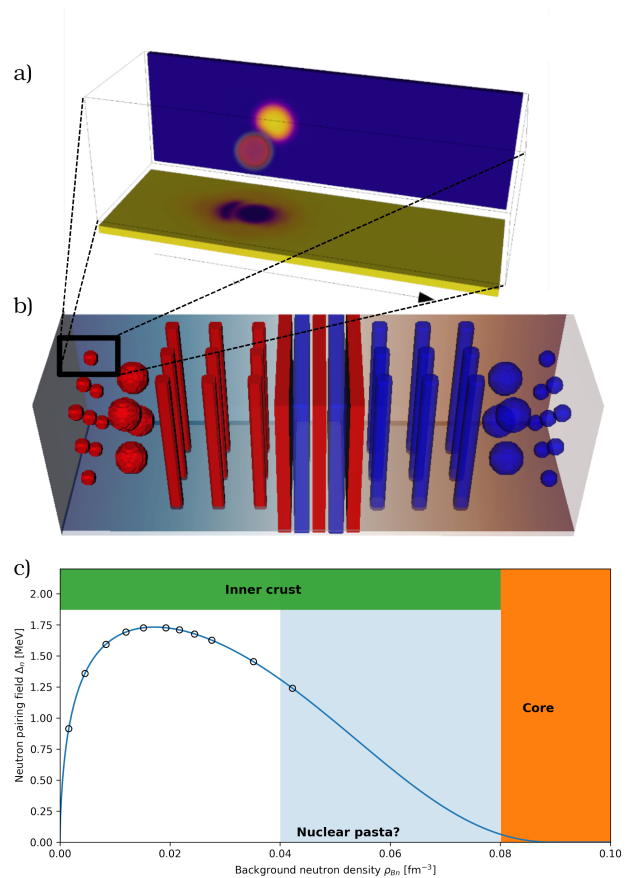


FIG. 1. In panel a) we show the numerical setup considered in this work: a nucleus accelerating to the right through a neutron superfluid medium. The red sphere in the middle shows the proton density. The map at the bottom shows the neutron pairing field $\Delta_n(\mathbf{r})$ for $x = 0$ cut. The map beyond shows the neutron density $\rho_n(\mathbf{r})$ for $y = 0$ cut. In panel b) a schematic picture of the geometrical structures in the inner crust of a neutron star. Our region of interest corresponds to cases where protons form quasi spherical self-bound impurities. At higher densities, exotic configurations such as rods or slabs referred to as “nuclear pasta” might be present. Red surfaces represent schematically boundaries of proton clusters in dilute neutron matter, while blue surfaces represent protonic holes in a dense nuclear matter. In panel c) we show the 1S_0 neutron pairing gap Δ_n in neutron matter as a function of the background neutron density ρ_{Bn} [35], on which the pairing part of the BSk functional is based. The circles indicate densities for which we extract the dynamical properties of the impurities.

tions, one needs to solve, have the same structure as the Hartree-Fock-Bogoliubov equations with local fields. Their generic structure is (for brevity we omit position and time dependence)

$$i\hbar \frac{\partial}{\partial t} \begin{pmatrix} u_{k\uparrow} \\ u_{k\downarrow} \\ v_{k\uparrow} \\ v_{k\downarrow} \end{pmatrix} = \begin{pmatrix} h_{\uparrow\uparrow} & h_{\uparrow\downarrow} & 0 & \Delta \\ h_{\downarrow\uparrow} & h_{\downarrow\downarrow} & -\Delta & 0 \\ 0 & -\Delta^* & -h_{\uparrow\uparrow}^* & -h_{\uparrow\downarrow}^* \\ \Delta^* & 0 & -h_{\downarrow\uparrow}^* & -h_{\downarrow\downarrow}^* \end{pmatrix} \begin{pmatrix} u_{k\uparrow} \\ u_{k\downarrow} \\ v_{k\uparrow} \\ v_{k\downarrow} \end{pmatrix}, \quad (1)$$

where $[u_{k\uparrow}, u_{k\downarrow}, v_{k\uparrow}, v_{k\downarrow}]^T$ are four component quasiparticle orbitals: mixtures of particles ($v_{k\sigma}$) and holes ($u_{k\sigma}$) with a set of quantum numbers k and spin projections $\sigma = \{\uparrow, \downarrow\}$. The $h_{\sigma\sigma'}$ and Δ are single particle hamiltonian and pairing potential, respectively. In the case of nuclear problems, the terms $h_{\uparrow\downarrow}$ and $h_{\downarrow\uparrow}$ arise due to spin-orbit interaction. It is imperative in the description of nuclei; for example, it is responsible for the correct reproduction of nuclear magic numbers. On the other hand, the spin-orbit term does not contribute in homogeneous matter, and was shown to be very small in the crust of neutron stars [30]. On the technical level, the presence of $h_{\uparrow\downarrow}$ and $h_{\downarrow\uparrow}$ terms significantly increases the computation cost. There are numerical packages for nuclear dynamics, like LISE [40], that are optimized toward studies of nuclear reactions. We optimize our toolkit towards applications to neutron stars, and in this context, the ability to model phenomena in large volumes (compared to the size of nuclei in vacuum) is of major importance. Due to predicted small spatial variability of nuclear densities, the spin-orbit coupling is of secondary importance. For this reason, we neglect the spin-orbit contribution. The computations savings emerging from this simplification will allow us to consider volumes exceeding 100^3 fm^3 .

Under the assumptions $h_{\uparrow\downarrow} = h_{\downarrow\uparrow} = 0$ and $h_{\uparrow\uparrow} = h_{\downarrow\downarrow} = h$, it is sufficient to solve the Hartree-Fock-Bogoliubov equations for a two-component vector [41]

$$i\hbar \frac{\partial}{\partial t} \begin{pmatrix} u_{q,k\uparrow} \\ v_{q,k\downarrow} \end{pmatrix} = \begin{pmatrix} h_q & \Delta_q \\ \Delta_q^* & -h_q^* \end{pmatrix} \begin{pmatrix} u_{q,k\uparrow} \\ v_{q,k\downarrow} \end{pmatrix}, \quad (2)$$

where we added an extra index $q = n, p$ to indicate that these equations must be solved for neutrons and protons respectively. There is another set of equations for components $\{u_{q,k\downarrow}, v_{q,k\uparrow}\}$. However, there is no need to solve them independently, as the solution can be obtained from $\{u_{q,k\uparrow}, v_{q,k\downarrow}\}$ via suitable transformation [42].

To solve the time-dependent equations (2) one needs to provide an initial configuration specified by $\{u_{q,k\uparrow}(\mathbf{r}, 0), v_{q,k\downarrow}(\mathbf{r}, 0)\}$. It is usually obtained as a solution of static HFB equations (for clarity, we omit in notation the position dependence)

$$\begin{pmatrix} h_q & \Delta_q \\ \Delta_q^* & -h_q^* \end{pmatrix} \begin{pmatrix} u_{q,k\uparrow} \\ v_{q,k\downarrow} \end{pmatrix} = E_{q,k} \begin{pmatrix} u_{q,k\uparrow} \\ v_{q,k\downarrow} \end{pmatrix}. \quad (3)$$

Solving these equations self-consistently for the nonuniform matter in the inner crust of a neutron star, by itself, constitutes a challenging problem, and most of the results presented in the literature are limited to this type of calculations with the further approximation of a spherical WS cell, as e.g. in Refs. [43–45].

The core of every DFT method is an energy density functional $\mathcal{E}[\rho_q, \nu_q, \tau_q, \mathbf{j}_q]$ that depends on the normal densities (ρ_q), anomalous densities (ν_q), kinetic densities (τ_q), currents (\mathbf{j}_q) and in our case also on the gradients of density $\nabla\rho_q$. The densities are constructed from the

quasiparticle states

$$\rho_q = 2 \sum_k [|v_{q,k\downarrow}|^2 f_T(-E_{q,k}) + |u_{q,k\uparrow}|^2 f_T(E_{q,k})], \quad (4)$$

$$\tau_q = 2 \sum_k [|\nabla v_{q,k\downarrow}|^2 f_T(-E_{q,k}) + |\nabla u_{q,k\uparrow}|^2 f_T(E_{q,k})], \quad (5)$$

$$\nu_q = 2 \sum_k u_{q,k\uparrow} v_{q,k\downarrow}^* (f_T(-E_{q,k}) - f_T(E_{q,k})), \quad (6)$$

$$\begin{aligned} \mathbf{j}_q &= 2 \sum_k \text{Im} [v_{q,k\downarrow} \nabla v_{q,k\downarrow}^*] f_T(-E_{q,k}) + \\ &+ 2 \sum_k \text{Im} [u_{q,k\uparrow} \nabla u_{q,k\uparrow}^*] f_T(E_{q,k}). \end{aligned} \quad (7)$$

The factor two in the above equations comes from the spin degeneracy of neutrons and protons. The summation over k is restricted only to the interval below the cutoff energy $0 < E_{q,k} < E_{\text{cut}}$. The thermal occupation factors (k_B is Boltzmann constant)

$$f_T(E) = \left[1 + \exp\left(\frac{E}{k_B T}\right) \right]^{-1}, \quad (8)$$

have been introduced to W-BSk Toolkit to allow investigations at finite temperatures.

The energy of the system has a generic form

$$\begin{aligned} E &= \int \mathcal{E}[\rho_q, \nu_q, \tau_q, \mathbf{j}_q] d\mathbf{r} - \sum_{q=n,p} \int (\mu_q - V_q^{(\text{ext})}) \rho_q d\mathbf{r} \\ &- \frac{1}{2} \sum_{q=n,p} \int (\Delta_q^{(\text{ext})} \nu_q^* + \text{h.c.}) d\mathbf{r} \\ &- \hbar \sum_{q=n,p} \int \mathbf{v}_q^{(\text{ext})} \cdot \mathbf{j}_q d\mathbf{r}. \end{aligned} \quad (9)$$

The first term in the above expression is the intrinsic energy of the system. The remaining three terms are introduced as generalized Lagrange multipliers. In general external field $V_q^{(\text{ext})}$, external pairing field $\Delta_q^{(\text{ext})}$, and external velocity field $\mathbf{v}_q^{(\text{ext})}$ are position and time dependent. They are coupled to normal ρ_q , anomalous ν_q and current \mathbf{j}_q densities, respectively, and allow to control them depending on the problem considered. Note that from the $V_q^{(\text{ext})}$, we have extracted the constant part μ_q that has the meaning of the chemical potential. If $V_q^{(\text{ext})}(\mathbf{r}, t) = 0$ one recognizes that the associated term reduces to well know form $-\mu_q N_q$, where $N_q = \int \rho_q(\mathbf{r}, t) d\mathbf{r}$. The introduction of generalized Lagrange multipliers make the toolkit applicable to a plethora of problems. For example, setting $\mathbf{v}_q^{(\text{ext})} = \mathbf{\Omega} \times \mathbf{r}$ results in the requirement of putting our system into rotation with angular velocity $\mathbf{\Omega}$. In this work, we will use the external potential $V_q^{(\text{ext})}(\mathbf{r}, t)$ to simulate the presence of an external electric field.

In this particular study, we adopted the energy density functional BSk31 [28]. This functional from the

Brussels-Montreal family was constructed from generalized Skyrme effective interactions [36] and has the following form:

$$\begin{aligned} \mathcal{E}[\rho_q, \vec{\nabla}\rho_q, \nu_q, \tau_q, \mathbf{j}_q] \\ = \frac{\hbar^2}{2M_n}\tau_n + \frac{\hbar^2}{2M_p}\tau_p + \mathcal{E}_\tau(\rho_q, \tau_q, \mathbf{j}_q) \end{aligned} \quad (10a)$$

$$+ \mathcal{E}_\rho(\rho_q) + \mathcal{E}_{\Delta\rho}(\rho_q, \vec{\nabla}\rho_q) \quad (10b)$$

$$+ \mathcal{E}_\pi(\rho_q, \vec{\nabla}\rho_q, \nu_q) + \mathcal{E}_{\text{Coul}}(\rho_p). \quad (10c)$$

The different terms above have the following meaning. In line (10a), the first two terms correspond to the kinetic energy density of protons and neutrons, while \mathcal{E}_τ is the energy density arising from the momentum-dependent part of the effective interaction. This last term is responsible for the density-dependent effective mass of the nucleons (in contrast to the effective mass of the impurity that we study in this paper) and for the mutual neutron-proton entrainment effects due to current-current couplings [46, 47]. The two terms in line (10b) contribute to the mean-field potential felt by a nucleon due to its interactions with the dense background and its spatial fluctuations. The last two terms in (10c) account for pairing (see Appendix A) and Coulomb interactions.

The single-particle mean-fields h_q and pairing potentials Δ_q , are defined for a given density functional \mathcal{E} through variation over proper densities:

$$\begin{aligned} h_q = -\nabla \frac{\delta\mathcal{E}}{\delta\tau_q} \nabla + \frac{\delta\mathcal{E}}{\delta\rho_q} - (\mu_q - V_q^{(\text{ext})}) \\ - \frac{i}{2} \left\{ \frac{\delta\mathcal{E}}{\delta\mathbf{j}_q} - \hbar \mathbf{v}_q^{(\text{ext})}, \nabla \right\}, \end{aligned} \quad (11)$$

$$\Delta_q = -2 \frac{\delta\mathcal{E}}{\delta\nu_q^*} + \Delta_q^{(\text{ext})}. \quad (12)$$

According to our shorthand notation the term $\delta\mathcal{E}/\delta\mathbf{j}_q$ describes components x, y, z arising from the variation of the energy with respect to the current density components j_{qx}, j_{qy}, j_{qz} . respectively. One can now recognize the mathematical complexity of the problem: the potentials h_q and Δ_q depend on densities (4)-(7), which in turn are expressed through the quasiparticle states $\{u_{q,k\uparrow}, v_{q,k\downarrow}\}$. They need to be obtained from the equations (2) and (3) that are defined via h_q and Δ_q .

To tackle the problem, we designed a software `W-BSk Toolkit`. It is based on the numerical engine of `W-SLDA Toolkit` [48], constructed for ultracold atomic gases. The `W-SLDA` engine has been already applied to various problems. Landscape of problems encapsulate: quantum vortices [49–52], solitons [53], exotic states in spin-imbalanced gases [54–57], Josephson junctions [58], Higgs modes [59], quantum turbulence [60, 61]. In the first stage, we adapted the code for pure neutron matter and applied it to investigations of quantum vortices at finite temperatures [62] using the functional BSk31 [28]. Here, we accomplished the second stage, extending it to take into account the presence of protons. In the present

study, we use the same functional BSk31. We also assume the whole system is electrically charge neutral; the positive proton charge is compensating by the presence of a uniform electron gas. The full expression of the functional \mathcal{E} and the associated mean fields can be found in Appendix A.

Cartesian lattice is used to discretize the space (2) and (3). Consequently the quasiparticle wavefunctions are expressed on a mesh of size $N_x \times N_y \times N_z$ with lattice spacings $\Delta x, \Delta y$ and Δz , respectively. Tests indicated that $\Delta x \approx 1.25$ fm provides already high-quality representation [40, 63]. The equations are solved imposing periodic boundary conditions. The lattice spacing provides a natural energy cut-off scale $E_{\text{cut}} = \hbar^2\pi^2/(2m\Delta x^2)$. It is located in energy window $E_{\text{cut}} \approx (130 - 200)$ MeV for lattice spacings spanning (1.00 – 1.25)fm, which is significantly larger than the Fermi energy of nucleons. That implies that the number of considered states is also much larger than the number of simulated particles. The large values of the energy cut-off are required in order to maintain the trustable evolution of the nuclear system [13, 64, 65]. The lattice representation allows for efficient utilization of spectral methods for computation of derivatives [66]. These are high-accuracy methods with the associated numerical cost comparable to finite-difference methods (precisely, the computation cost is set by the efficiency of a fast Fourier transform). The time integration of Eq. (2) is done via the multi-step Adams-Bashforth-Moulton (ABM) method of the 5-th order. This integrator generates stable and accurate length trajectories $\sim 10^4$ fm/c. The robustness of the time integrator with respect to the perturbations of the initial states has been demonstrated in [67]. The static problem (3) is solved by a series of direct diagonalizations supported by the ELPA library [68–70]. Convergence of the self-consistent loop is greatly improved by utilization of the Broyden algorithm [71]. The solvers for static and time-dependent problems are parallelized by MPI protocol, and GPUs are used to achieve the highest computation performance. The implementation supports both nVidia and AMD accelerators. The code is scalable up to the largest HPC systems today available for open science. For example, when running on tier-0 systems, like LUMI [72], it can deal with problems formulated on the lattice of size 100^3 [73]. The implementation is released in the form of an open-source code. It is accessible via the web page [29], so everyone can inspect the implementation and reuse solutions derived within this `W-BSk Toolkit` project.

III. APPLICATION: NUCLEAR IMPURITY MOVING IN A NEUTRON SUPERFLUID

In the inner crust of a cold neutron star, matter is expected to exhibit various kinds of structures [74]. As a demonstration of the capabilities offered by the DFT framework, let us consider the range of average nucleon

number densities for which protons and neutrons bind into quasispherical clusters immersed in a neutron superfluid bath. The description of the dynamical properties of such impurity poses a challenging theoretical problem, which requires to describe properly the energy and momentum transfer between the impurity and the surrounding neutrons. One of the fundamental characteristics of the impurity is its inertia, whose modifications by the medium can be described by an effective mass. The problem of determining effective masses has in itself a long history, considered already by Landau [75] and Fröhlich [76] in the context of electrons in solids. The situation considered here resembles the problem of a heavy impurity for which the general solution still evades theoretical description [77, 78]. In the most general formulation, it concerns a heavy impurity with a mass $M \gg m$, where m is the mass of fermions forming the environment, moving with a velocity $V \ll v_F$, where v_F is the Fermi velocity of the environment particles. The interactions of the impurity are supposed to be of short-range $d \approx n^{-1/3}$, where n is the number density of particles in the environment. The goal is to integrate out the fermionic degrees of freedom and arrive at some effective equation of motion for the impurity alone. Such an equation should contain the change of the impurity mass by the medium and a dissipative term describing the irreversible energy flow between the impurity and the environment. Already at this stage, the situation is quite complicated since without the presence of a gap in the energy spectrum of the excitations of the medium, there is no natural scale that would allow defining quantitatively departure from the adiabatic limit. Indeed, in such cases, the motion of the impurity with an arbitrarily small velocity would induce many particle-hole excitations in the medium, leading to strong dissipation. In the extreme case, it leads to a predicted paradox of a complete motionless regime, which is a direct consequence of Anderson orthogonality catastrophe [79, 80]. Another parameter that governs the dynamics of the impurity is its radius R as compared to the average interparticle distance d in the medium. In the case $R \ll n^{-1/3}$, the s -wave scattering dominates the particle-impurity interaction, whereas in the regime $R \gg n^{-1/3}$ the impurity can be treated as a semiclassical scatterer. The latter corresponds to the considered case of a nuclear impurity in neutron matter.

The neutron matter inside the crust is expected to be superfluid. In such a case, a clear distinction between adiabatic frictionless motion, and dissipative regimes should be observed due to the presence of an energy gap in the quasiparticle excitation spectrum. Although it eliminates some of the above-mentioned difficulties, the problem remains complex. The impurity is made of protons tightly bound by nuclear forces and to which some neutrons are also attached. Most of those neutrons would be unbound in vacuum. They are held together with the proton cluster only because continuum states are already occupied. In other words, the impurity is closely connected to the neutron environment and would not exist without. More-

over, the impurity is penetrable for neutrons. For these reasons, the effective characteristics of the impurity are not well established, and various predictions have been made. Most studies were carried out in the framework of classical hydrodynamics [81–85]. A quantum mechanical estimation of the effective mass of an impurity was first attempted in Ref. [86]. These calculations, however, were not self-consistent, and superfluidity was not explicitly taken into account. In all these cases, the motion of the impurity was assumed to remain stationary. This hypothesis only holds if the relative velocity of the impurity with respect to the neutron superfluid is sufficiently small. In reality, various kinds of perturbations can appear, including the nucleation of quantized vortices. This calls for a fully self-consistent, time-dependent quantum treatment. Such treatment for 1D geometry (slabs) in the inner crust of a neutron star has been recently reported [87, 88].

Here we demonstrate that the time-dependent DFT formalism provides a complementary method, which offers a better insight into the physical mechanisms associated with a moving impurity. These mechanisms are hard to describe within the static approach, especially for 3D geometry. For example, conceptually simple calculations of an impurity moving through the neutron superfluid, deliver an abundance of physical information related to the effective mass of the impurity, the presence of dissipative forces, or even insight into the problem of the nucleation of quantum vortices in the interiors of neutron stars.

IV. NUMERICAL EXPERIMENT

We consider a small matter element of the inner crust: a nuclear cluster immersed in a sea of superfluid neutrons at zero temperature $T \rightarrow 0$, see Fig. 1(a). The most stable clusters expected to be present in broad regions of the inner crust are very neutron-rich zirconium isotopes with proton number $Z = 40$ [30]. In order to investigate its dynamical properties, we accelerate it through the superfluid medium by applying a constant electric field in a z direction $\mathbf{E} = [0, 0, E_z]$. As a results, protons move due to the electric force $\mathbf{F} = Ze\mathbf{E}$, dragging a certain number of neutrons. Technically, the constant force is modeled by a linear external potential that couples only to protons

$$V_p^{(\text{ext})}(\mathbf{r}) = -\frac{1}{Z}\mathbf{F} \cdot \mathbf{r}. \quad (13)$$

The numerical simulation consists of three main steps: i) finding a self-consistent solution for the ground state of the cluster; ii) extracting the initial wave function $\{u_{q,k\uparrow}(\mathbf{r}, 0), v_{q,k\downarrow}(\mathbf{r}, 0)\}$; iii) evolving the system in time. In the first step, we solve self-consistently the HFB equations (3) with the constraints $N_p = Z = 40$ and the density of neutrons far from the nucleus ρ_{Bn} . This is achieved by properly adjusting the chemical potentials

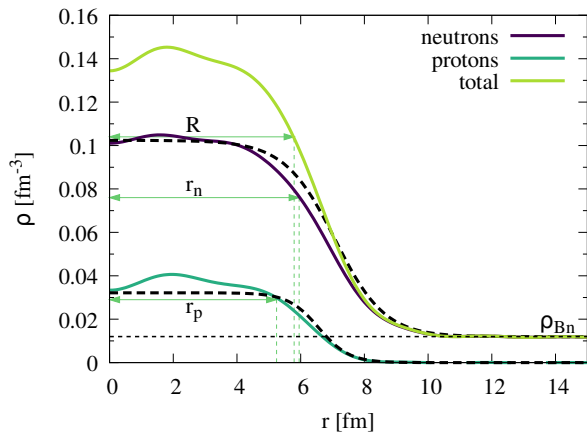


FIG. 2. Typical density profile for a ${}_{40}\text{Zr}$ cluster existing in the layer of the inner crust of a neutron star at the average nucleon density $\bar{\rho} = 0.01481\text{fm}^{-3}$. Far from the cluster, neutrons are uniformly distributed with a density $\rho_{Bn} = 0.01196\text{fm}^{-3}$. Solutions of the HFB equations (solid lines) are compared with fourth-order extended Thomas-Fermi calculations (dashed lines) [89]. By r_p and r_n we denote the root mean square radii of protons and neutrons (after subtracting the neutron background density).

μ_q . We solve the equations without any geometrical restriction on a uniform cubic grid $32 \times 32 \times 32$ with a lattice spacing $\Delta x = \Delta y = \Delta z = 1.25$ fm. The resulting volume 40^3fm^3 is large enough to saturate the values of bulk neutron density to the desired value ρ_{Bn} that corresponds to the layer in the inner crust with average density $\bar{\rho}$ (see Table I). The selected values of ρ_{Bn} are indicated by circles in Fig. 1(c). The algorithm converges to a spherically symmetric distribution of protons and neutrons in all considered cases. Examples of 1D density distributions obtained for $\rho_{Bn} = 0.01196\text{fm}^{-3}$ are shown in Fig. 2. We compare our results with semi-classical predictions represented by dashed black lines and based on fourth-order extended Thomas-Fermi calculations in spherical Wigner-Seitz cells [89]. In this approach, the shell and pairing effects were neglected and the nucleon-density distributions were parametrized; thus, the density distributions are almost flat inside the impurity, contrary to self-consistent calculations.

From the static calculations, we may estimate the number of bound neutrons as follows:

$$N_{\text{bound}} = \int (\rho_n(\mathbf{r}) - \rho_{Bn}) d\mathbf{r}. \quad (14)$$

This definition gives the proper result in the limit $\rho_{Bn} \rightarrow 0$ (the nucleus in the vacuum), and it provides an estimate for the effective mass of the impurity according to the formula

$$M_{\text{eff}}^{(s)} = Zm_p + N_{\text{bound}}m_n, \quad (15)$$

where m_p and m_n are masses of protons and neutrons, respectively. In the calculations, we assume that $m_p \approx$

$m_n \approx 939.57\text{MeV}/c^2$. To determine the size of the impurity we use the root mean square radius

$$R = \sqrt{\langle R^2 \rangle} = \sqrt{\frac{\int \rho_{\text{tot}}(\mathbf{r})r^2 d\mathbf{r}}{\int \rho_{\text{tot}}(\mathbf{r}) d\mathbf{r}}}, \quad (16)$$

where $\rho_{\text{tot}}(\mathbf{r}) = \rho_n(\mathbf{r}) - \rho_{Bn} + \rho_p(\mathbf{r})$. Similarly, we can define the neutron and proton root mean square radii associated with bound neutrons r_n and protons r_p , using the densities $\rho_n(\mathbf{r}) - \rho_{Bn}$, and $\rho_p(\mathbf{r})$, respectively. These quantities are depicted in Fig. 2. The tests provide satisfactory agreement with the results reported in Ref [89]. Note that the calculations presented here, apart from neglecting the spin-orbit coupling, contain all contributions to the energy density functional (nuclear, pairing, and Coulomb terms) taken into account in a fully self-consistent manner (there are no other hidden approximations). The good agreement with the independent calculations demonstrates the correctness of the energy functional implementation within our toolkit.

Next, in the stage ii), we triple the volume of the system by adding two cubes (each of volume 40^3fm^3) filled with uniform superfluid neutron matter of density ρ_{Bn} to the side of the solution from stage i). In this way, we prepare a sufficient space for the motion of the impurity, which will be performed in volume $40^2 \times 120 \text{fm}^3$. (The tools allowing for the manipulations of static solutions are also included in the toolkit). Note that one does not need very accurately converged ground state, for the time evolution procedure. Since we are interested in non-equilibrium dynamics, it is enough to be fairly close to the ground state, i.e. within an excitation energy that is small compared to excitation energies generated by the dynamics. Therefore, in the stage (ii) it is sufficient to perform just a few iterations of the self-consistent method, which at this stage becomes costly since we are now diagonalizing HFB matrices of size $2 \times 32^2 \times 96 = 196,608$. (We estimated that the energy is minimized up to the accuracy of the order of keV per nucleon.) At the end of this process, the wavefunctions $\{u_{q,k\uparrow}(\mathbf{r}, 0), v_{q,k\downarrow}(\mathbf{r}, 0)\}$ are stored. The total number of states (for protons and neutrons) in energy interval $E_{q,k} \in [0, E_c = 130 \text{MeV}]$ exceeds slightly hundred thousand, while total number of nucleons is from 456 for the lowest ($\rho_{Bn} \approx 0.002\text{fm}^{-3}$) up to 8150 for the highest ($\rho_{Bn} \approx 0.051\text{fm}^{-3}$) densities.

The resulting quantum states are subsequently evolved (step iii), using the time-dependent HFB equations (2). At this stage, we introduce a constant electric field along the longest side of the simulation box, that we denote as z , via Eq. (13). We turn on the electric field $E_z(t)$ gradually within the time interval $\Delta t = 10\text{fm}/c$ (For explicit protocol see Appendix B). The equations of motion are integrated with a time step $dt = 0.1 \text{fm}/c$. We monitor the conservation of the particle number and the total energy (after the external electric field is turned on, see Appendix B), which is satisfied with high accuracy (the particle number is conserved within a precision of $10^{-6}\%$

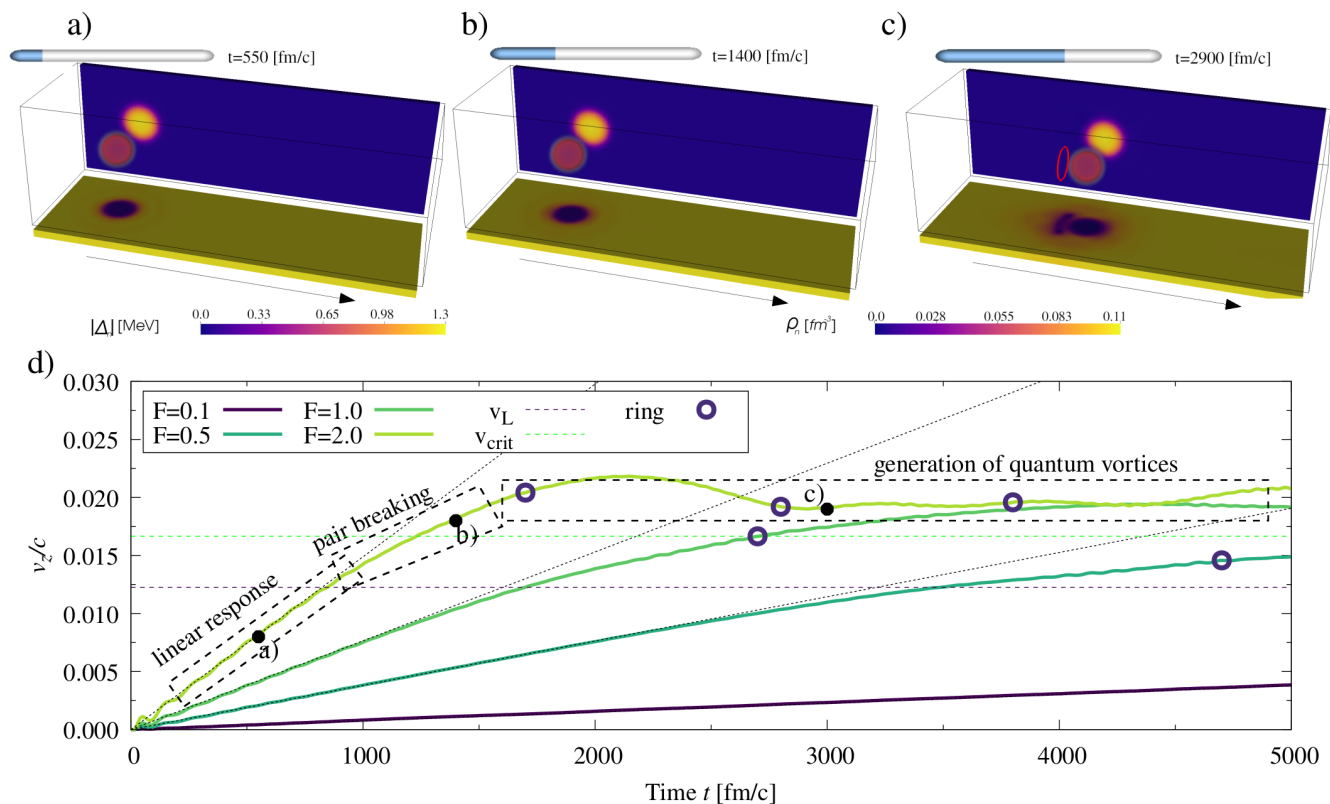


FIG. 3. a)–c) Snapshots of the impurity dynamics for selected times (550, 1400, and 2900 fm/c) as indicated in panel d). Each frame shows proton density (red sphere in the box), neutron density cross-section ρ_n (behind), modulus of the neutron pairing field $|\Delta_n|$ (bottom). The black arrow indicates the direction of a constant electric field. See Supplementary Material for the full movie [90]. d) The velocity of the center of the mass of protons dragged in superfluid neutrons of density $\rho_{Bn} \approx 0.0045$ fm for different forces F (measured in MeV/fm). For this density, we observe three distinct regimes of dynamics: linear response, dissipative dynamics induced by the breaking of Cooper pairs, and quantum vortex proliferation for certain moments (denoted by blue circles). The vortices are created for velocities above the Landau velocity v_L (blue dashed line). Impurity velocities tend to the critical velocity v_{crit} (green dashed line). Black dotted lines show the linear fit for the short duration of dynamics.

and the total energy with a precision from 0.5% up to 0.001% over the trajectory length $\Delta t = 5000$ fm/c, depending on the density). The simulations were executed for different strengths of $F \equiv ZeE_z$. Sample frames from simulations are shown in Figs 1(a) and 3(a–c). All other technical settings are provided in the Supplementary Material [90].

The real-time dynamics provides insight into the evolution of the densities (4)–(7). From them, we can obtain the desired observables. The time evolution of the position of the center of mass of protons

$$\mathbf{R}_{cm}(t) = \frac{1}{Z} \int \rho_p(\mathbf{r}, t) \mathbf{r} d\mathbf{r} \quad (17)$$

immediately reveals the existence of different dynamical regimes. In Fig. 3(d), we show the z component of the velocity of the center of mass (the velocity along the x and y directions is zero)

$$\mathbf{v}_{cm}(t) = \frac{d\mathbf{R}_{cm}(t)}{dt} = [0, 0, v_z(t)] \quad (18)$$

for a few values of external forces F . As long as the velocity is not too large, it changes linearly with time $v_z(t) \sim a_z t$, except for the initial stage of the evolution, discussed in Appendix C, which is due to the excitation of the collective mode being an analogue of isovector Giant Dipole Resonance (IGDR). Apart from the effect of IGDR excitation, which can be minimized by decreasing the rate of switching on the electric field, the regime is essentially dissipationless, and the impurity moves according to Newton's law $F = M_{eff} a_z$. Since F is the control parameter and a_z can be accurately extracted from the simulated data, we obtain an unequivocal method of extracting the effective mass. Once the impurity is accelerated above a threshold value (which is density-dependent), the constant external force no longer induces a uniformly accelerated motion. This signals that additional forces start to act on the impurity. This regime provides insight into dissipative effects, due to irreversible coupling of the impurity with the superfluid bath. These conceptually simple numerical experiments involving time evolution turn out to provide a plethora of

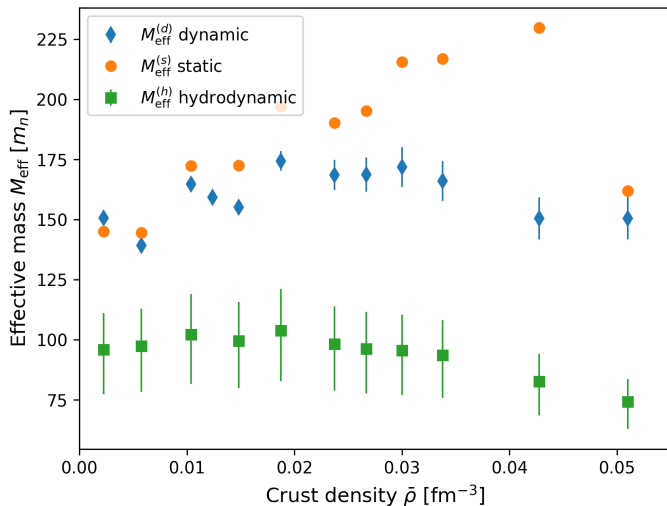


FIG. 4. The effective mass of the nucleus calculated with different approaches: dynamic $M_{\text{eff}}^{(d)}$, static $M_{\text{eff}}^{(s)}$, hydrodynamic $M_{\text{eff}}^{(h)}$. The details, including how we determine the error bars are explained in the main text. The hydrodynamic approximation gives qualitative behavior, while static calculations match results in the low-density regime.

information, that is either hard or impossible to extract from static calculations.

V. EFFECTIVE MASS

For all considered densities, we found that initially, the impurity moves with a constant acceleration, irrespective of the applied constant force F . The initial linear increase of the impurity velocity is a consequence of the superfluidity. In the regime where the superfluid velocity does not exceed Landau’s critical velocity, no quasiparticle can be excited and the motion is dissipationless [91, 92]. This peculiar feature is crucial for the successful extraction of the effective mass. Namely, the presence of an energy gap in the excitation spectrum of the system makes the determination of effective mass a well-posed question in contrast to the normal fluids, where particle-hole excitations occur at arbitrary small velocity, making the problem of disentangling reversible and irreversible energy exchange between impurity and environment practically impossible. In Fig. 3(d), we plot the velocity of the center of mass of protons extracted from the simulations, together with fitted linear functions $a_z t$ for the initial part of the trajectory. As expected, the ratio $M_{\text{eff}}^{(d)} = a_z/F$ turns out to be almost independent of the force. We show the fitted values of effective mass $M_{\text{eff}}^{(d)}$ for various densities in Fig. 4 as blue diamonds. The error bars indicate the differences of effective mass $M_{\text{eff}}^{(d)}$ extracted for different magnitudes of the force accelerating the nucleus. The effective mass is significantly higher than Zm_p , and the difference $M_{\text{eff}}^{(d)} - Zm_p$ is related to the number of neutrons

that are effectively bound (including those entrained by protons).

The extracted effective mass $M_{\text{eff}}^{(d)}$ can be compared to other approaches. The simplest one, and most commonly adopted, relies on the formula (15). The key idea is to distinguish between bound and free neutrons based on the spatial properties of the single-particle density distribution. This approach has semi-classical roots as it provides a reasonable answer in the limit of $k_F R \rightarrow \infty$ and also under the assumption that the length scale of spatial variations of density is large compared to the Fermi wavelength. In such a case, contributions coming from shell effects and resonant states can be neglected. Both these assumptions can be questioned in the context of neutron-star crust. The other approach is based on hydrodynamic considerations. The modification of the mass of a moving impurity comes from the excitation of the flow in the superfluid medium, which is assumed to be incompressible and irrotational. Under such assumptions, the flow that results merely from mass conservation can be easily extracted. Namely, if the impurity is chosen to be a sphere of radius R with a sharp surface filled with fluid of density ρ_{in} , whereas the outside density of fluid ρ_{out} is associated with the bulk neutrons, then the energy cost of exciting the superfluid flow scales with the velocity V as $E \sim V^2$. The proportionality coefficient quantifies the effective mass, and according to [83] it reads

$$M_{\text{eff}}^{(h)} = \frac{4}{3}\pi R^3 m_n \frac{(\rho_{\text{in}} - \rho_{\text{out}})^2}{\rho_{\text{in}} + 2\rho_{\text{out}}}. \quad (19)$$

One can see that the definition (19) simplifies in two important limits. In the absence of impurity (the matter is uniform $\rho_{\text{in}} = \rho_{\text{out}}$), the effective mass is zero. On the other hand, when the impurity is in vacuum ($\rho_{\text{out}} = 0$ and ρ_{in} equals nuclear matter saturation density $\rho_0 \approx 0.16 \text{ fm}^{-3}$) the effective mass reduces to the “bare” mass obtained from the product of the nucleon mass by number of nucleons. To compare this formula with the effective mass extracted from TDDFT we have identified densities $\rho_{\text{in}}, \rho_{\text{out}}$ as densities at the center of the impurity and the corner of the numerical box, respectively. Similarly, we have used the root-mean-square radius given by Eq. (16) to determine R . Since the surface of the realistic cluster is not sharp, we have estimated the uncertainty of the effective mass estimation within the hydrodynamics approach from the values corresponding to $90\%R$ and $110\%R$.

In Fig. 4 we compare the effective masses obtained within different approaches, together with their uncertainties. The dynamical approach based on TDDFT does not rely on any assumption concerning the size and shape of the impurity. As expected, the static prescription $M_{\text{eff}}^{(s)}$ matches the dynamical ones in the regimes of low densities $\bar{\rho} \lesssim 0.01 \text{ fm}^{-3}$. At higher densities, $\bar{\rho} \gtrsim 0.03 \text{ fm}^{-3}$, discrepancy can be observed. In static calculations, the size of the impurity therefore also its effective mass grows with density, while in the dynamical approach the effec-

tive mass tends to saturate. This indicates that the simple division between bound and unbound neutrons, based on geometrical arguments only, becomes questionable. In contrast, the hydrodynamic approach systematically underestimates the effective mass. This can be understood from the fact that the hydrodynamics approach takes into account only one effect related to the superfluid motion, namely, the excitation of incompressible and irrotational flow. Note also that the applicability of the hydrodynamics approach can be questioned, if we recall that the impurity size R is of the same order as the most important length scales of the neutron superfluid, namely the coherence length $\xi = \hbar k_{F_n} / (\pi \Delta_n m_n)$, where the Fermi wave vector is given by $k_{F_n} = (3\pi^2 \rho_n)^{1/3}$. One would need $\xi \ll R$ for hydrodynamics to be quantitatively accurate. For this reason, the assumption that the impurity can be described in terms of superfluid hydrodynamics is too crude.

The effective mass of an impurity moving in a dense nucleon background has been recently shown to play an important role in the formation of clusters in a hot newly born neutron star [93]. The clusterization of matter does not only depend on surface and Coulomb effects, but also on the (uncorrelated) translational motion of clusters, which in turn is modified by the medium through the renormalization of their mass. Although the motions of individual clusters are suppressed after the crust crystallizes, their collective motion can still be described in terms of an effective mass [94]. However, the origin of this effective mass is different: it is due to coherent Bragg scattering of free neutrons by the nuclear lattice [95, 96]. This effective mass is a key microscopic inputs for modeling the dynamics of neutron stars and for interpreting various observed phenomena, such as pulsar glitches [97]. The calculation is left for future applications of the toolkit.

VI. DISSIPATION

One of the hallmarks of a superfluid state is the existence of dissipationless flow. A typical example is an obstacle moving in a superfluid without creating any excitation. The above statement is correct under the assumption of zero temperature $T = 0$ and sufficiently small velocities $v < v_L$ of moving obstacles. This characteristic threshold velocity v_L is the so-called Landau velocity. For a uniform neutron superfluid of density $\rho_n = k_{F_n}^3 / (3\pi^2)$, it is approximately given by the well-known formula from the BCS theory [98] (see Ref. [91] for the exact treatment in the nuclear context)

$$v_L = \frac{\Delta_n}{\hbar k_{F_n}}, \quad (20)$$

where k_F is the Fermi wave vector. At this velocity, there is enough of kinetic energy to break a Cooper pair or equivalently excite a quasiparticle above the energy gap. In Fig. 3, we see that the uniformly accelerated motion

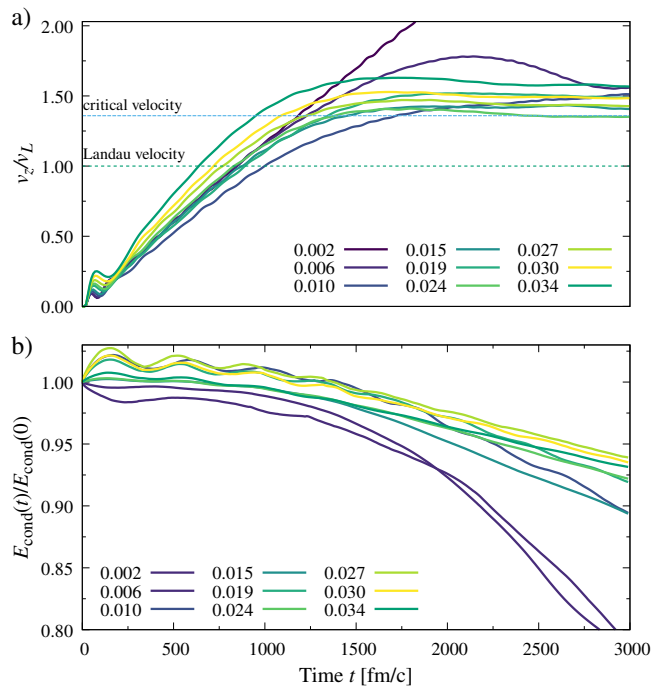


FIG. 5. a) The velocity of the impurity as a function of time for different densities, normalized to the respective values of the Landau velocity. The data series corresponds to force $F=2\text{MeV}/\text{fm}$. By dashed and dotted lines, we indicate two characteristic velocity scales. b) The condensation energy E_{cond} relative to its initial value as a function of time for the same data series as in panel a).

is lost once the impurity velocity approaches v_L . The comparison for various densities is shown in Fig. 5(a).

To demonstrate that the Cooper pair breaking is responsible for the dissipative dynamics once v_L is reached, let us consider the condensation energy of neutron Cooper pairs defined as

$$E_{\text{cond}}(t) = \int \frac{3}{8} \frac{|\Delta_n(\mathbf{r}, t)|^2}{\varepsilon_{F_n}(\mathbf{r}, t)} \rho_n(\mathbf{r}, t) d\mathbf{r} \quad (21)$$

where $\varepsilon_{F_n}(\mathbf{r}, t) = \hbar^2 [3\pi^2 \rho_n(\mathbf{r}, t)]^{2/3} / [2m_n^*(\mathbf{r}, t)]$ is the local Fermi energy of neutrons, and m_n^* is effective mass of a neutron. In the case of a uniform system, it reduces to $3\Delta_n^2 N_n / (8\varepsilon_{F_n})$, which is a standard formula known from the BCS theory. The quantity (21) is displayed in Fig. 5(b). For velocities $v_z < v_L$, the velocity of the impurity increases linearly while the condensation energy remains fairly constant. Once the Landau's velocity is reached, the condensation energy starts to drop. It is worth noting that the onset of Cooper pair breaking does not match exactly the velocity v_L . In general, one needs to consider the velocity field of neutrons. It can be computed by noting that $\mathbf{j}_n(\mathbf{r}, t) = \rho_n(\mathbf{r}, t) \mathbf{v}_n(\mathbf{r}, t)$. The extracted $\mathbf{v}_n(\mathbf{r}, t)$ at three selected time instants is displayed in panels (a)-(c) of Fig. 6. The blue color shows regions with a velocity field below the threshold value $v_n(r) < v_L$, white color indicate regions, where it be-

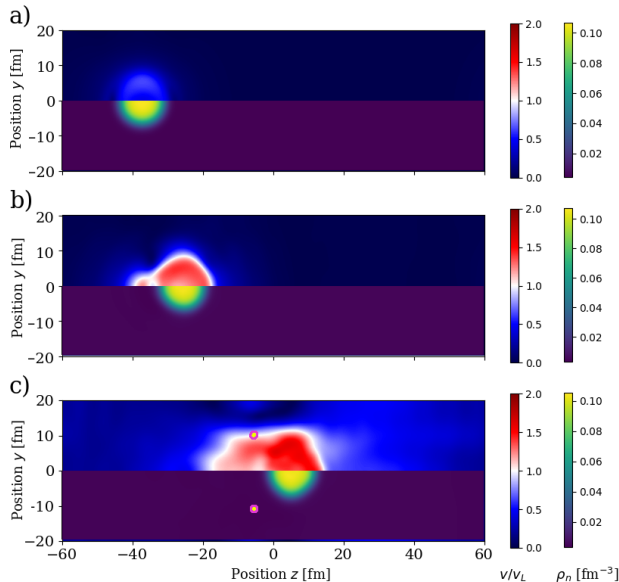


FIG. 6. Each panel presents the neutron density cross section through $x = 0$ (lower part), and local velocity in units of bulk Landau velocity (upper part). The consecutive panels are taken at times 550, 1400, and 2900 fm/c, which correspond to Fig. 3(a)–(c). a) in the linear response regime mainly the impurity is moving. b) in the breaking pair regime the free neutrons in the vicinity of impurity are affected. c) in the turbulent regime a large volume of neutrons is affected. Two points shown behind the impurity (at $z \approx -5$ fm) are the cross section of the vortex ring generated in this regime.

comes comparable to $v_n(r) \approx v_L$, and the red color shows regions where the velocity exceeds v_L . The figure shows clearly that the process of destroying the Cooper pairs takes place in the vicinity of the impurity. The relation between v_n and velocity of the impurity v_z is shown in Fig. 5(a). Inside the impurity, the neutron velocity v_n coincides with the velocity v_z of the impurity.

There is another striking feature, which can be seen in Fig. 5(b): almost in all cases, the speed of the impurity saturates at the value

$$v_{\text{crit}} = \frac{e}{2} v_L \approx 1.4 v_L. \quad (22)$$

(The lowest density $\rho_{Bn} = 0.002$ is close to the limit of an impurity moving in vacuum, where the coupling to the environment is not expected). In Ref [91], it was shown under the assumption that the system is uniform, and if the superfluid velocity exceeds Landau’s velocity, the system enters into a so-called gapless regime. It is a regime where a normal fluid (defined by quasiparticle excitations) coexists with the superfluid, even at zero temperature [91]. The superfluidity in the uniform system is destroyed once the superfluid velocity reaches v_{crit} . Although the system considered here is not homogeneous, our numerical simulations indicate that v_{crit} remains the characteristic velocity scale. However, the normal com-

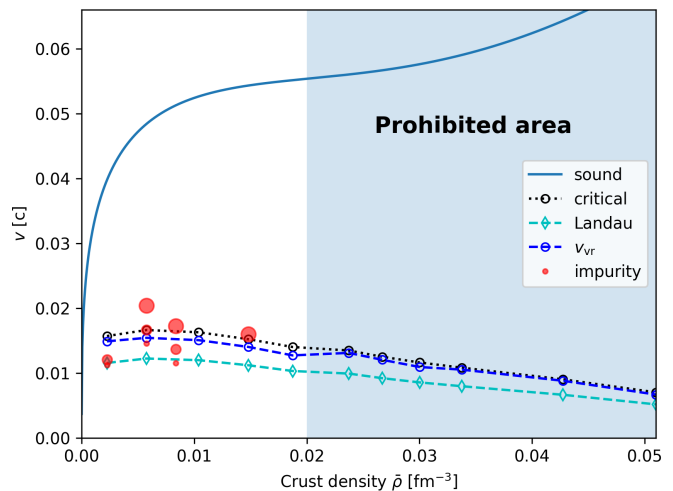


FIG. 7. The velocity scales in the system. The speed of sound (solid line) of the system is a few times larger than the Landau velocity v_L (black and green dashed lines). We plot the hydrodynamic velocity of a vortex ring v_{vr} with the dashed blue line. By red dots, we denote the nucleus velocity at which the vortex ring is created of three different sizes for different forces (MeV/fm): $F = 0.5, 1,$ and 2 , respectively. The vortex rings are not produced in the blue area on the right side.

ponent appears in the form of a vortex ring around the moving nucleus; see Fig. 3(c).

The vortex-shedding process has been observed experimentally in superfluid He [99, 100] and ultracold atomic gases [101, 102]. It was also simulated numerically using the Gross-Pitaevskii equation (see examples in reported in Refs. [103–105]). In these studies, the obstacle was unpenetrable and much bigger than the coherence length. In the case of nuclear impurity, the situation is different. First of all, there is no clear separation of scales. Second, the impurity is penetrable for neutrons. Yet, in our microscopic simulations, we find successful vortex ring generation cases. For example, in the cases presented in Fig. 3, we denoted the vortex rings appearance with circles. One can notice that the creation of a vortex ring occurred always when the velocity of a nucleus/impurity exceeds the Landau velocity v_L . These vortices may be generated one by one, preventing the impurity to move faster than v_{crit} . With the increase of the magnitude of the force F , the rate of vortex creation increases, which we may understand by noting that the rate of energy pumping into the system depends on the force $\sim \mathbf{F} \cdot \mathbf{v}$. The velocities for which we have detected the vortex nucleation are summarized in Fig. 7.

Exceeding Landau’s velocity for the relative flow generated by impurity and the sea of neutrons, is not the only criterion that must be fulfilled. Once the vortex is nucleated, it must propagate with a slower velocity than the impurity, to be able to detach. The velocity of a vor-

text ring in the hydrodynamic regime is given by [106]:

$$v_{\text{vr}}(r) = \frac{1}{4\pi r} \frac{h}{2m_n} \left(\ln \frac{8r}{r_{\text{core}}} - \alpha \right), \quad (23)$$

where we used the fact that the circulation unit is given by $\Gamma = h/2m_n$. The coefficient α depends on the selected vortex core model; typically, $\alpha \approx 1/2$. It assumes that the vortex ring is a smooth circle. In reality, the line can be wiggled due to Kelvin wave excitations that modify the velocity of the vortex ring, which are also seen in our simulations. The hydrodynamic formula is derived for the limit of the vortex ring radius r , being much larger than the vortex core radius r_{core} . In Fig. 7 we show the velocity predicted by formula (23), where we use $\alpha = 1/2$, radius $r = R$ given by formula Eq (16), and $r_{\text{core}} = \xi$. It turns out that this velocity is very close to the critical velocity v_{crit} , which provides another argument indicating that it is one of the important velocity scales for the construction of effective models.

Systematic studies for various densities show that vortex rings are not always formed. We have not detected nucleation of vortices for densities above $\bar{\rho} > 0.02 \text{fm}^{-3}$. This threshold value coincides with densities at which the coherence ξ becomes larger than the impurity size. The coherence length $\xi = \hbar k_{\text{F}n} / (\pi \Delta_n m_n)$ of superfluid neutrons has a nontrivial behavior. The Fermi momentum $k_{\text{F}n}$ is an increasing function of density ρ_n , while Δ_n has a maximum at $\rho_n \approx 0.017 \text{fm}^{-3}$. The minimum coherence length is at density $\rho_n \approx 0.006 \text{fm}^{-3}$. The size of the impurity depends on the density as well. In Fig. 7, we indicate by blue color the density range where the coherence length is slightly larger than the nucleus radius $\xi > 120\%R$. Clearly, in this regime, we do not detect the vortex nucleation process: one cannot generate a vortex of radius that is smaller than the size of the vortex core.

The numerical simulations demonstrate that vortex rings can be nucleated in the crust of a neutron star in the layers, where the density of superfluid neutrons is below 0.02fm^{-3} provided the relative superfluid velocity exceeds (at least locally) Landau's velocity v_L . Studies of superfluid helium show that the injection of vortex rings is a very efficient way of generating quantum turbulence [107–110]. While our microscopic simulations cannot provide a definite answer on whether quantum turbulence can be present in neutron stars, they clearly show how quantum turbulence could develop at the smallest scale. This may have important implications for the global dynamics of neutron stars and the interpretation of sudden spin-ups seen as frequency glitches in some pulsars [111]. Although superfluidity is expected to play a major role, the actual triggering mechanism remains uncertain. Quantum turbulence could be one of them [112].

VII. SUMMARY

To conclude, we have demonstrated that the quality of present DFT techniques combined with modern HPC

solutions allows for the investigation of microscopic properties of nuclear systems and their quantum dynamics at the smallest scales relevant to neutron-star crust. This is a critical step to construct global effective hydrodynamical models of neutron stars by averaging the local dynamics at smaller scales. Matter element exceeding the size of WS cells can be considered for both static and time-dependent HFB calculations without any symmetry restriction. In particular, time-dependent DFT may shed a new light on problems inaccessible so far through static approaches. Full 3D time evolutions without making any assumption on the weakness of external perturbations allow to investigate a plethora of aspects of neutron-star crusts. As an illustration of the possibilities offered by the toolkit, we have considered a simple numerical experiment in which a nuclear impurity is accelerated through a neutron superfluid medium by a constant force. Results of our simulations have provided new insight into the effective mass of the impurity, the characteristic velocity scales, the dissipative channels, and the mechanism for generation of topological defects. In particular, we have shown that low lying excitation modes, which are analogues of IGDR in atomic nuclei, can accompany the motion of impurity and therefore have to be included in any low energy description of neutron-star crust.

Collecting such vast information has been possible by combining both static and time-dependent approaches: the system has been evolved from an initial configuration generated by self-consistent HFB calculations. The problem addressed here is only one from a large variety of questions, related to neutron stars, which can be investigated in a similar way. Among others, we can list the dynamics of quantum vortices in neutron-star crust (proof of concepts were already demonstrated in Refs. [113, 114]), pycnonuclear fusion processes, properties of exotic phases like nuclear pasta, and many others [115, 116]. Together with this paper, we make the associated toolkit publicly available for the community to allow for such studies.

The abundance of open problems that are related to neutron stars is large. Collective effort within a unified approach is needed to foster progress. In particular, new functionals are being elaborated to fulfill the specific needs of time-dependent simulations of the kind presented here. Namely, the so-called family of functionals Brussels-Skyrme-on-a-Grid (BSkG) is optimized towards applications involving calculations on 3D meshes [117–120], as presented in this paper. We strongly advocate for the further developments of a unified set of tools for the microscopic study of neutron stars in the future. This work aims at stimulating this effort and providing a software library in which other functionals can be easily implemented by making the code open-source.

ACKNOWLEDGEMENTS

DP acknowledges the hospitality from Université Libre de Bruxelles. We thank Nikolai Shchepochin for sharing cluster profiles data used for comparison. This work was financially supported by the (Polish) National Science Center Grants No. 2021/40/C/ST2/00072 (DP), 2021/43/B/ST2/01191 (PM), 2022/45/B/ST2/00358 (GW, AZ). This work was also supported by the Fonds de la Recherche Scientifique (Belgium) under Grant No. PDR T.004320 (NC). We acknowledge PRACE for awarding us access to resource Piz Daint based in Switzerland at Swiss National Supercomputing Centre (CSCS), decision No. 2021240031. We acknowledge Polish high-performance computing infrastructure PLGrid for awarding this project access to the LUMI supercomputer, owned by the EuroHPC Joint Undertaking, hosted by CSC (Finland) and the LUMI consortium through PLL/2022/03/016433.

Author contributions: Construction of the W-BSK Toolkit : DP, GW; numerical calculations: DP, AZ; results analysis: DP, AZ, GW. All authors contributed to research planning, interpretation of the results and manuscript writing.

Data reproducibility: Reproducibility packs are provided in the Supplemental Material [90]. They provide the complete information needed to reproduce the results presented in this paper.

Appendix A: Brussels-Montreal functionals

Here we provide the technical details concerning the type of functionals we are using, and the expression of the mean fields implemented into W-BSK Toolkit. Our code can handle semi-local functionals from the Brussels-Montreal family based on generalized Skyrme effective interactions with density-dependent t_1 and t_2 terms for the normal part [36], and a density-dependent contact interaction for the pairing part [38]. In this work, we have adopted the BSk31 functional, whose parametrization can be found in Ref. [28]. The expressions for the energy density and the mean fields in the absence of currents can be found in Ref. [36]. The additional terms depending on the currents were explicitly given in our previous work [62] for the special case of pure neutron matter. Here we provide expressions for arbitrary composition.

Below we introduce the isospin index $\iota = 0, 1$ for isoscalar and isovector quantities, respectively. Isoscalar quantities (also written without any subscript) are sums over neutrons and protons (e.g., $\rho_0 \equiv \rho_n + \rho_p$), while isovector quantities are differences between neutrons and protons (e.g., $\rho_1 \equiv \rho_n - \rho_p$). The different terms of the nuclear energy density functional take the following forms [121]:

$$\mathcal{E}_\rho = \sum_\iota C_\iota^\rho[\rho] \rho_\iota^2, \quad (\text{A1})$$

$$\mathcal{E}_\tau = \sum_\iota C_\iota^\tau[\rho] (\rho_\iota \tau_\iota - \mathbf{j}_\iota^2), \quad (\text{A2})$$

$$\mathcal{E}_{\Delta\rho} = \sum_\iota C_\iota^{\Delta\rho} \rho_\iota \Delta\rho_\iota + C_\iota^{\nabla\rho}[\rho] \Delta\rho_\iota. \quad (\text{A3})$$

The coupling coefficients are related to the parameters of the generalized Skyrme interaction as

$$\begin{aligned} C_0^\rho[\rho] &= \frac{3}{8}t_0 + \frac{3}{48}t_3\rho^\alpha, \\ C_1^\rho[\rho] &= -\frac{1}{4}t_0\left(\frac{1}{2} + x_0\right) - \frac{1}{24}t_3\left(\frac{1}{2} + x_3\right)\rho^\alpha, \\ C_0^\tau[\rho] &= \frac{3}{16}t_1 + \frac{1}{4}t_2\left(\frac{5}{4} + x_2\right) \\ &\quad + \frac{3}{16}t_4\rho^\beta + \frac{1}{4}t_5\left(\frac{5}{4} + x_5\right)\rho^\gamma, \\ C_1^\tau[\rho] &= -\frac{1}{8}t_1\left(\frac{1}{2} + x_1\right) + \frac{1}{8}t_2\left(\frac{1}{2} + x_2\right) \\ &\quad - \frac{1}{8}t_4\rho^\beta\left(\frac{1}{2} + x_4\right) + \frac{1}{8}t_5\left(\frac{1}{2} + x_5\right)\rho^\gamma \\ C_0^{\Delta\rho}[\rho] &= -\frac{9}{64}t_1 + \frac{1}{16}t_2\left(\frac{5}{4} + x_2\right) - \frac{3}{32}t_4\rho^\beta \\ C_1^{\Delta\rho}[\rho] &= \frac{3}{32}t_1\left(\frac{1}{2} + x_1\right) + \frac{1}{32}t_2\left(\frac{1}{2} + x_2\right) \\ &\quad + \frac{1}{16}t_4\left(\frac{1}{2} + x_4\right)\rho^\beta \end{aligned} \quad (\text{A4})$$

$$C_0^{\nabla\rho}[\rho] = \frac{3}{64}t_4\rho^\beta - \frac{1}{16}t_5\left(\frac{5}{4} + x_5\right)\rho^\gamma \quad (\text{A5})$$

$$C_1^{\nabla\rho}[\rho] = -\frac{1}{32}t_4\left(\frac{1}{2} + x_4\right)\rho^\beta - \frac{1}{32}t_5\left(\frac{1}{2} + x_5\right)\rho^\gamma. \quad (\text{A6})$$

The pairing contribution to the energy density functional is given by Eq. (9) of Ref. [28]:

$$\begin{aligned} \mathcal{E}_\pi &= \frac{1}{4}f_n^\pm (v^{\pi n}(\rho_n, \rho_p) + \kappa_n |\nabla\rho_n|^2) \nu_n^2 \\ &\quad + \frac{1}{4}f_p^\pm (v^{\pi p}(\rho_n, \rho_p) + \kappa_p |\nabla\rho_p|^2) \nu_p^2, \end{aligned} \quad (\text{A7})$$

where $f_q^\pm \approx 1$. In our calculations, we set $f_q^\pm = 1$ and we drop the gradient terms. The pairing strengths $v^{\pi q}(\rho_n, \rho_p)$ were constructed so as to reproduce exactly the 1S_0 pairing gaps obtained in Ref. [35] in pure neutron matter and symmetric nuclear matter from extended Brueckner-Hartree-Fock calculations including medium polarization and self-energy effects. We adopt the analytical approximation given in Ref. [39]:

$$v^{\pi q} = -\frac{8\pi^2}{\sqrt{\mu_q}} B_q^{3/2} \left[2 \ln \left(\frac{2\mu_q}{|\Delta_q|} \right) + \Lambda \left(\frac{\varepsilon_\Lambda}{\mu_q} \right) \right]^{-1}, \quad (\text{A8})$$

where μ_q is the chemical potential, ε_Λ is the cutoff and

$$\Lambda(x) = \ln(16x) + 2\sqrt{1+x} - 2\ln(1 + \sqrt{1+x}) - 4. \quad (\text{A9})$$

The single-particle Hamiltonian h_q can be obtained by varying the energy density functional \mathcal{E} with respect to the various densities and currents (4)–(7), and reads

$$h_q = U_q^\rho + U_q^{\Delta\rho} + U_q^\tau + U_q^\pi - \nabla B_q \nabla - \frac{i}{2} \{ \mathbf{A}_q, \nabla \}. \quad (\text{A10})$$

The first four terms are scalar potentials coming from variation over the density ρ_q

$$U_q^\rho = \frac{\partial \mathcal{E}_\rho}{\partial \rho_q}, \quad (\text{A11})$$

$$U_q^\tau = \frac{\partial \mathcal{E}_\tau}{\partial \rho_q}, \quad (\text{A12})$$

$$U_q^{\Delta\rho} = \frac{\partial \mathcal{E}_{\Delta\rho}}{\partial \rho_q} - \nabla \cdot \frac{\partial \mathcal{E}_{\Delta\rho}}{\partial (\nabla \rho_q)} + \Delta \frac{\partial \mathcal{E}_{\Delta\rho}}{\partial (\Delta \rho_q)}, \quad (\text{A13})$$

$$U_q^\pi = \frac{\partial \mathcal{E}_\pi}{\partial \rho_q} - \nabla \cdot \frac{\partial \mathcal{E}_\pi}{\partial (\nabla \rho_q)}. \quad (\text{A14})$$

We checked that U_q^π is very small compared to other terms, therefore we neglect it in our calculations. The field B_q arises from the dependence of the functional on the kinetic density τ_q :

$$B_q = \frac{\hbar^2}{2M_q} + \frac{\partial \mathcal{E}_\tau}{\partial \tau_q}. \quad (\text{A15})$$

The last term is a vector potential induced by the presence of a current \mathbf{j}_q :

$$\mathbf{A}_q = \frac{\partial \mathcal{E}_\tau}{\partial \mathbf{j}_q}. \quad (\text{A16})$$

The various mean fields are expressible as

$$B_q = \frac{\hbar^2}{2M_q} + C_0^\tau \rho + C_1^\tau (\rho_q - \rho_{q'}), \quad (\text{A17})$$

$$\mathbf{A}_q = -2C_0^\tau \mathbf{j} - 2C_1^\tau (\mathbf{j}_q - \mathbf{j}_{q'}), \quad (\text{A18})$$

$$U_q^\rho = \frac{dC_0^\rho}{d\rho} \rho_n^2 + \frac{dC_1^\rho}{d\rho} (\rho_q - \rho_{q'})^2 + 2\rho C_0^\rho + 2(\rho_q - \rho_{q'}) C_1^\rho, \quad (\text{A19})$$

$$U_q^\tau = C_0^\tau \tau + C_1^\tau (\tau_q - \tau_{q'}) + \frac{dC_0^\tau}{d\rho} (\rho\tau - \mathbf{j}^2) + \frac{dC_1^\tau}{d\rho} [(\rho_q - \rho_{q'}) (\tau_q - \tau_{q'}) - (\mathbf{j}_q - \mathbf{j}_{q'})^2], \quad (\text{A20})$$

$$U_q^{\Delta\rho} = 2C_0^{\Delta\rho} \Delta\rho + 2C_1^{\Delta\rho} (\Delta\rho_q - \Delta\rho_{q'}) + \frac{dC_0^{\nabla\rho}}{d\rho} \Delta\rho + \frac{dC_1^{\nabla\rho}}{d\rho} (\Delta\rho_q - \Delta\rho_{q'}) + \nabla \cdot \left(\frac{dC_0^{\nabla\rho}}{d\rho} \nabla \rho \right) + \nabla \cdot \left(\frac{dC_1^{\nabla\rho}}{d\rho} \nabla (\rho_q - \rho_{q'}) \right). \quad (\text{A21})$$

Here q' means the complementary nucleon species to q (if $q = n$, $q' = p$ and vice versa).

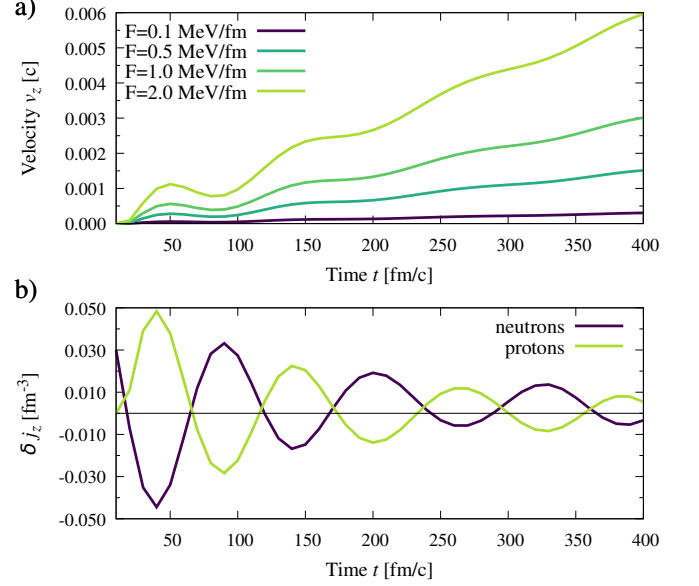


FIG. 8. a) The zoom for short time from Fig. 3d). One can observe damped oscillations on top of a linear increase in velocity. b) Neutron and proton currents along z direction for $F = 2\text{MeV/fm}$. We removed a linear increase of the current seen in a) that is not relevant for the effect. See the main text for the details.

Appendix B: Protocol for turning on the electric field

The static solutions are generated with no external potentials and are used as starting points for time-dependent considerations. To initialize dynamics, we turn on the electric field in the following way:

$$E_z(t) = \begin{cases} 0 & \text{if } t < t_1, \\ E_z s(t - t_1, t_2 - t_1) & \text{if } t_1 < t < t_2, \\ E_z & \text{if } t_2 < t, \end{cases} \quad (\text{B1})$$

where t is time, and t_1, t_2 denote over which we rise smoothly the electric field from the initial up to the final value. The switching function s that models the rising of the field is:

$$s(t, \Delta t) = \frac{1}{2} \left\{ 1 + \tanh \left[\tan \left(\pi \frac{t}{\Delta t} - \frac{\pi}{2} \right) \right] \right\}. \quad (\text{B2})$$

We used $\Delta t = t_2 - t_1 = 10\text{fm}/c$ in our calculations.

Appendix C: Giant Dipole Resonance in neutron matter

If one looks closer at the first moments of our simulation, the increase of velocity $v_z(t)$ is not linear. For example, in Fig. 8(a), we present a zoom-in of the initial stage of motion from Fig. 3(d). On top of linear behavior, there are damped oscillations. These oscillations are generated as a side effect of our numerical setup; however, they have a well-defined physical origin.

The oscillations are caused by the fact that we 'turn on' the electric field E_z , Eq. (B1), once the static solution, representing impurity at rest, is generated. Although we do not do it instantaneously but smoothly increase the interaction during a finite but short time Δt . The smaller the period Δt or, the larger the force F , the larger becomes the amplitude of oscillations. Since only protons couple to the electric potential, they start to move as first. Next, they begin to drag neutrons bound to them through nuclear forces. Such a scenario gives rise to an excitation of an analogue of isovector giant dipole resonance (GDR) mode in our system. It is the basic excitation mode in nuclear systems, where protons vibrate (practically harmonically) against neutrons [122, 123]. GDR is not dissipationless mode, resulting in its finite width due to coupling to more complex nuclear configurations or to the continuum [124]. As evidence,

that indeed we induce GDR, we plot the currents for neutrons and protons in Fig. 8(b), but with subtracted constant linear flow of the whole nucleus. We see that protons and neutrons are out of phase. Moreover, we can see from the figure that the period of oscillations is approximately $T \approx 100\text{fm}/c$. This is consistent with the phenomenological formula for the GDR frequency $\Omega_{\text{GDR}} = 0.39A^{-1/3} c/\text{fm}$ [125], even though it has been designed for finite-size nuclei in a vacuum not interacting with neutron superfluid. The formula with $A = 140$ provides the oscillation period to be about $84\text{fm}/c$ which is of the same order as observed.

Appendix D

We provide the table with a summary of characteristic quantities for considered cases.

-
- [1] Chris L Fryer, "Mass limits for black hole formation," *The Astrophysical Journal* **522**, 413 (1999).
 - [2] J. M. Lattimer and M. Prakash, "The physics of neutron stars," *Science* **304**, 536–542 (2004), <https://www.science.org/doi/pdf/10.1126/science.1090720>.
 - [3] D. G. Yakovlev and C. J. Pethick, "Neutron Star Cooling," *Ann. Rev. Astron. Astrophys.* **42**, 169–210 (2004).
 - [4] A. B. Migdal, "Superfluidity and the moments of inertia of nuclei," *Nucl. Phys.* **13**, 655–674 (1959).
 - [5] N. Chamel, "Superfluidity and Superconductivity in Neutron Stars," *J. Astrophys. Astron.* **38**, 43 (2017).
 - [6] Armen Sedrakian and John W. Clark, "Superfluidity in nuclear systems and neutron stars," *Eur. Phys. J. A* **55**, 167 (2019).
 - [7] Nils Andersson, "A superfluid perspective on neutron star dynamics," *Universe* **7** (2021), 10.3390/universe7010017.
 - [8] J. Engel, "Intrinsic-density functionals," *Phys. Rev. C* **75**, 014306 (2007).
 - [9] Jérémie Messud, Michael Bender, and Eric Suraud, "Density functional theory and kohn-sham scheme for self-bound systems," *Phys. Rev. C* **80**, 054314 (2009).
 - [10] T Duguet and J Sadoudi, "Breaking and restoring symmetries within the nuclear energy density functional method," *Journal of Physics G: Nuclear and Particle Physics* **37**, 064009 (2010).
 - [11] T. Nakatsukasa, K. Matsuyanagi, M. Matsuo, and K. Yabana, "Time-dependent density functional description of nuclear dynamics," *Rev. Mod. Phys.* **88**, 045004 (2016).
 - [12] G. Colò, "Nuclear Density Functional Theory," *Adv. Phys. X* **5**, 1740061 (2020).
 - [13] P. Magierski, "Nuclear Reactions and Superfluid Time-Dependent Density Functional Theory," *Progress of Time-Dependent Nuclear Reaction Theory* **2**, 57–71 (2019).
 - [14] A. Bulgac, "Time-Dependent Density Functional Theory for Fermionic Superfluids: From Cold Atomic Gases - To Nuclei and Neutron Stars Crust," *Phys. Status Solidi (b)* **256**, 1800592 (2019).
 - [15] R. M. Dreizler and E. K. U. Gross, *Density Functional Theory: An Approach to the Quantum Many-body Problem* (Springer, 1990).
 - [16] C. Fiolhais, F. Nogueira and M. A. L. Marques, ed., *A Primer in Density Functional Theory* (Springer Berlin Heidelberg, 2003).
 - [17] M. A.L. Marques, N. T. Maitra, F. M.S. Nogueira, E.K.U. Gross and A. Rubio, ed., *Fundamentals of Time-Dependent Density Functional Theory* (Springer Berlin Heidelberg, 2012).
 - [18] N. D. Mermin, "Thermal properties of the inhomogeneous electron gas," *Phys. Rev.* **137**, A1441–A1443 (1965).
 - [19] H. Eschrig, "T>0 ensemble-state Density Functional Theory via Legendre transform," *Phys. Rev. B* **82**, 205120 (2010).
 - [20] S. Pittalis, C. R. Proetto, A. Floris, A. Sanna, C. Bersier, K. Burke, and E. K. U. Gross, "Exact Conditions in Finite-Temperature Density Functional Theory," *Phys. Rev. Lett.* **107**, 163001 (2011).
 - [21] L. N. Oliveira, E. K. U. Gross and W. Kohn, "Density Functional Theory for Superconductors," *Phys. Rev. Lett.* **60**, 2430–2433 (1988).
 - [22] O. J. Wacker, R. Kümmel and E. K. U. Gross, "Time-Dependent Density Functional Theory for Superconductors," *Phys. Rev. Lett.* **73**, 2915–2918 (1994).
 - [23] M. Lüders, M. A. L. Marques, N. N. Lathiotakis, A. Floris, G. Profeta, L. Fast, A. Continenza, S. Massidda and E. K. U. Gross, "Ab initio theory of superconductivity. I. Density functional formalism and approximate functionals," *Phys. Rev. B* **72**, 024545 (2005).
 - [24] M. A. L. Marques, M. Lüders, N. N. Lathiotakis, G. Profeta, A. Floris, L. Fast, A. Continenza, E. K. U. Gross and S. Massidda, "Ab initio theory of superconductivity. ii. application to elemental metals," *Phys. Rev. B* **72**, 024546 (2005).
 - [25] A. Bulgac, "Local Density Functional Theory for superfluid fermionic systems: The unitary gas," *Phys. Rev. A* **76**, 040502 (2007).

$\bar{\rho}[\text{fm}^{-3}]$	$\rho_{Bn}[\text{fm}^{-3}]$	$\Delta_n[\text{MeV}]$	$k_F[\text{fm}^{-1}]$	$\varepsilon_F[\text{MeV}]$	$\varepsilon_F^*[\text{MeV}]$	N	$\xi[\text{fm}]$	$R[\text{fm}]$	$M_{\text{eff}}[m_n]$
0.0023	0.0016	0.826	0.363	2.723	2.694	376.6	5.79	5.32	150.75 \pm 1.8
0.0058	0.0045	1.236	0.512	5.436	5.301	934.4	5.47	5.21	139.30 \pm 1.0
0.0104	0.0084	1.483	0.628	8.165	7.840	1696.8	5.58	5.64	164.70 \pm 3.1
0.0148	0.0120	1.562	0.707	10.37	9.839	2385.3	5.98	5.79	155.25 \pm 2.9
0.0187	0.0152	1.557	0.766	12.15	11.421	3032.5	6.49	6.21	174.45 \pm 4.1
0.0237	0.0193	1.621	0.829	14.24	13.248	3789.3	6.75	5.28	168.55 \pm 6.3
0.0267	0.0217	1.566	0.863	15.42	14.268	4258.0	7.27	5.55	168.80 \pm 7.1
0.0300	0.0244	1.514	0.898	16.70	15.368	4847.1	7.82	7.46	171.85 \pm 8.3
0.0338	0.0276	1.467	0.935	18.10	16.558	5430.9	8.40	7.27	166.15 \pm 8.3
0.0428	0.0351	1.327	1.013	21.28	19.260	6925.0	10.1	8.71	150.50 \pm 8.8
0.0510	0.0422	1.097	1.077	24.05	21.618	8070.6	13.0	9.03	150.60 \pm 8.8

TABLE I. Quantities extracted from simulations for each density of the inner crust $\bar{\rho}$: ρ_{Bn} – bulk density of neutrons, Δ_n – pairing energy of neutrons, k_F – wave vector calculated for bulk density of neutrons, ε_F – Fermi energy, ε_F^* – Fermi energy calculated with regard to effective mass, N – number of neutrons, ξ – coherence length, R – radius of impurity, M_{eff} – effective mass of impurity.

- [26] Y. Yu and A. Bulgac, “Energy Density Functional Approach to Superfluid Nuclei,” *Phys. Rev. Lett.* **90**, 222501 (2003).
- [27] “Boosting materials modelling,” *Nat. Mater.* **15**, 365–365 (2016).
- [28] S. Goriely, N. Chamel and J. M. Pearson, “Further explorations of Skyrme–Hartree–Fock–Bogoliubov mass formulas. XVI. Inclusion of self-energy effects in pairing,” *Phys. Rev. C* **93**, 034337 (2016).
- [29] “W-BSK Toolkit,” <https://wbsk.fizyka.pw.edu.pl/>.
- [30] J. M. Pearson, N. Chamel, A. Y. Potekhin, A. F. Fantina, C. Ducoin, A. K. Dutta and S. Goriely, “Unified equations of state for cold non-accreting neutron stars with Brussels-Montreal functionals - I. Role of symmetry energy,” *Mon. Not. Roy. Astron. Soc.* **481**, 2994–3026 (2018).
- [31] O.-J. Wacker, R. Kümmel and E. K. U. Gross, “Time-Dependent Density Functional Theory for Superconductors,” *Phys. Rev. Lett.* **73**, 2915–2918 (1994).
- [32] S. Kurth, M. Marques, M. Lüders and E. K. U. Gross, “Local Density Approximation for Superconductors,” *Phys. Rev. Lett.* **83**, 2628–2631 (1999).
- [33] A. Bulgac, M. McNeil Forbes and P. Magierski, “The Unitary Fermi Gas: From Monte Carlo to Density Functionals,” in *Lecture Notes on Physics: The BCS-BEC Crossover and the Unitary Fermi Gas* (Springer-Verlag Berlin Heidelberg, 2012) p. 305.
- [34] A. Bulgac, “Time-Dependent Density Functional Theory and the Real-Time Dynamics of Fermi Superfluids,” *Annu. Rev. Nucl.* **63**, 97–121 (2013), <https://doi.org/10.1146/annurev-nucl-102212-170631>.
- [35] L. G. Cao, U. Lombardo and P. Schuck, “Screening effects in superfluid nuclear and neutron matter within brueckner theory,” *Phys. Rev. C* **74**, 064301 (2006).
- [36] N. Chamel, S. Goriely and J. M. Pearson, “Further explorations of Skyrme–Hartree–Fock–Bogoliubov mass formulas. XI. Stabilizing neutron stars against a ferromagnetic collapse,” *Phys. Rev. C* **80**, 065804 (2009).
- [37] N. Chamel, S. Goriely and J. M. Pearson, “Further explorations of Skyrme–Hartree–Fock–Bogoliubov mass formulas. IX: Constraint of pairing force to $^1\text{S}_0$ neutron-matter gap,” *Nucl. Phys. A* **812**, 72–98 (2008).
- [38] S. Goriely, N. Chamel and J. M. Pearson, “Skyrme–Hartree–Fock–Bogoliubov Nuclear Mass Formulas: Crossing the 0.6 MeV Accuracy Threshold with Microscopically Deduced Pairing,” *Phys. Rev. Lett.* **102**, 152503 (2009).
- [39] N. Chamel, “Effective contact pairing forces from realistic calculations in infinite homogeneous nuclear matter,” *Phys. Rev. C* **82**, 014313 (2010).
- [40] S. Jin, K. J. Roche, I. Stetcu, I. Abdurrahman and A. Bulgac, “The LISE package: Solvers for static and Time-Dependent Superfluid Local Density Approximation equations in three dimensions,” *Comput. Phys. Commun.* **269**, 108130 (2021).
- [41] A. Bulgac and M. McNeil Forbes, “Time-Dependent Superfluid Local-Density Approximation,” in *Quantum Gases: Finite Temperature and Non-Equilibrium Dynamics* (World Scientific, 2013) pp. 397–406.
- [42] J.-X. Zhu, *Bogoliubov-de Gennes Method and Its Applications* (Springer International Publishing, 2016).
- [43] M. Baldo, E. E. Saperstein, and S. V. Tolokonnikov, “A realistic model of superfluidity in the neutron star inner crust,” *European Physical Journal A* **32**, 97–108 (2007).
- [44] F. Grill, J. Margueron, and N. Sandulescu, “Cluster structure of the inner crust of neutron stars in the Hartree-Fock-Bogoliubov approach,” *Phys. Rev. C* **84**, 065801 (2011).
- [45] A. Pastore, M. Shelley, S. Baroni, and C. A. Diget, “A new statistical method for the structure of the inner crust of neutron stars,” *Journal of Physics G Nuclear Physics* **44**, 094003 (2017).
- [46] N. Chamel and V. Allard, “Entrainment effects in neutron-proton mixtures within the nuclear Energy-Density Functional Theory: Low-temperature limit,” *Phys. Rev. C* **100**, 065801 (2019).
- [47] V. Allard and N. Chamel, “Entrainment effects in neutron-proton mixtures within the nuclear energy-density functional theory. II. Finite temperatures and arbitrary currents,” *Phys. Rev. C* **103**, 025804 (2021).
- [48] “W-SLDA Toolkit,” <https://wsllda.fizyka.pw.edu.pl/>.

- [49] A. Bulgac, M. McNeil Forbes, M. M. Kelley, K. J. Roche and G. Wlazłowski, “Quantized superfluid vortex rings in the unitary fermi gas,” *Phys. Rev. Lett.* **112**, 025301 (2014).
- [50] A. Barresi, A. Boulet, P. Magierski and G. Wlazłowski, “Dissipative dynamics of quantum vortices in fermionic superfluid,” *Phys. Rev. Lett.* **130**, 043001 (2023).
- [51] M. Tylutki and G. Wlazłowski, “Universal aspects of vortex reconnections across the bcs-bec crossover,” *Phys. Rev. A* **103**, L051302 (2021).
- [52] J. Kopyciński, W. R. Pudelko and G. Wlazłowski, “Vortex lattice in spin-imbalanced unitary fermi gas,” *Phys. Rev. A* **104**, 053322 (2021).
- [53] G. Wlazłowski, K. Sekizawa, M. Marchwiany and P. Magierski, “Suppressed solitonic cascade in spin-imbalanced superfluid fermi gas,” *Phys. Rev. Lett.* **120**, 253002 (2018).
- [54] P. Magierski, B. Tüzemen, Buğra and G. Wlazłowski, “Spin-polarized droplets in the unitary fermi gas,” *Phys. Rev. A* **100**, 033613 (2019).
- [55] P. Magierski, G. Wlazłowski, A. Makowski and K. Kobuszewski, “Spin-polarized vortices with reversed circulation,” *Phys. Rev. A* **106**, 033322 (2022).
- [56] P. Magierski, B. Tüzemen and G. Wlazłowski, “Dynamics of spin-polarized impurity in ultracold fermi gas,” *Phys. Rev. A* **104**, 033304 (2021).
- [57] B. Tüzemen, T. Zawisłak, G. Wlazłowski and P. Magierski, “Disordered structures in ultracold spin-imbalanced fermi gas,” *New J. Phys.* **25**, 033013 (2023).
- [58] G. Wlazłowski, K. Xhani, M. Tylutki, N. P. Proukakis and P. Magierski, “Dissipation mechanisms in fermionic josephson junction,” *Phys. Rev. Lett.* **130**, 023003 (2023).
- [59] A. Barresi, A. Boulet, G. Wlazłowski and P. Magierski, “Generation and decay of higgs mode in a strongly interacting fermi gas,” *Sci. Rep.* **13** (2023), 10.1038/s41598-023-38176-9.
- [60] K. Hossain, K. Kobuszewski, M. McNeil Forbes, P. Magierski, K. Sekizawa and G. Wlazłowski, “Rotating quantum turbulence in the unitary fermi gas,” *Phys. Rev. A* **105**, 013304 (2022).
- [61] G. Wlazłowski, A. Bulgac, M. McNeil Forbes and K. J. Roche, “Life cycle of superfluid vortices and quantum turbulence in the unitary fermi gas,” *Phys. Rev. A* **91**, 031602 (2015).
- [62] D. Pęczak, N. Chamel, P. Magierski and G. Wlazłowski, “Properties of a quantum vortex in neutron matter at finite temperatures,” *Phys. Rev. C* **104**, 055801 (2021).
- [63] A. Bulgac, P. Magierski, K. J. Roche and I. Stetcu, “Induced fission of pu 240 within a real-time microscopic framework,” *Phys. Rev. Lett.* **116**, 122504 (2016).
- [64] P. Magierski, J. Grinevičute and K. Sekizawa, “Pairing Dynamics and Time-Dependent Density Functional Theory,” *Acta Phys. Pol. B* **49**, 281 (2018).
- [65] J. Grinevičute, P. Magierski, A. Bulgac, S. Jin and I. Stetcu, “Accuracy of Fission Dynamics Within the Time-Dependent Superfluid Local Density Approximation,” *Acta Phys. Pol. B* **49**, 591 (2018).
- [66] J. Shen, T. Tang and L.-L. Wang, *Spectral Methods* (Springer Berlin Heidelberg, 2011).
- [67] A. Bulgac, I. Abdurrahman and G. Wlazłowski, “Sensitivity of Time-Dependent Density Functional Theory to initial conditions,” *Phys. Rev. C* **105**, 044601 (2022).
- [68] A. Marek, V. Blum, R. Johanni, V. Havu, B. Lang, T. Auckenthaler, A. Heinecke, H.-J. Bungartz and H. Lederer, “The ELPA library: scalable parallel eigenvalue solutions for electronic structure theory and computational science,” *J. Phys. Condens. Matter* **26**, 213201 (2014).
- [69] V. W. Yu, J. Moussa, P. Küs, A. Marek, P. Messmer, M. Yoon, H. Lederer, Hermann and V. Blum, “GPU-acceleration of the ELPA2 distributed eigensolver for dense symmetric and hermitian eigenproblems,” *Comput. Phys. Commun.* **262**, 107808 (2021).
- [70] “ELPA (Eigenvalue solvers for Petaflop Applications),” <https://elpa.mpcdf.mpg.de>.
- [71] A. Baran, A. Bulgac, M. McNeil Forbes, G. Hagen, W. Nazarewicz, N. Schunck and M. V. Stoitsov, “Broyden’s method in nuclear structure calculations,” *Phys. Rev. C* **78**, 014318 (2008).
- [72] “LUMI supercomputer,” <https://www.lumi-supercomputer.eu/>.
- [73] G. Wlazłowski, M. M. Forbes, S. R. Sarkar, A. Marek and M. Szpindler, “Characterizing the cascade of energy in fermionic quantum turbulence: Pushing the limits of high-performance computing,” (2023), arXiv:2310.03341 [cond-mat.quant-gas].
- [74] D. Blaschke and N. Chamel, “Phases of Dense Matter in Compact Stars,” in *Astrophys. & Space Sci. Library*, Astrophys. & Space Sci. Library, Vol. 457, edited by L. Rezzolla, P. Pizzochero, D. I. Jones, N. Rea, and I. Vidaña (2018) p. 337.
- [75] L. D. Landau and S. I. Pekar, “Effective mass of a polaron,” *J. Exp. Theor. Phys.* **18**, 419 (1948).
- [76] H. Fröhlich, “Electrons in lattice fields,” *Adv. Phys.* **3**, 325–361 (1954).
- [77] A. Rosch, “Quantum-coherent transport of a heavy particle in a fermionic bath,” *Adv. Phys.* **48**, 295–394 (1999).
- [78] R. Schmidt, M. Knap, D. A. Ivanov, J.-S. You, M. Cetina and E. Demler, “Universal many-body response of heavy impurities coupled to a Fermi sea: a review of recent progress,” *Rep. Prog. Phys.* **81**, 024401 (2018).
- [79] P. W. Anderson, “Infrared catastrophe in fermi gases with local scattering potentials,” *Phys. Rev. Lett.* **18**, 1049–1051 (1967).
- [80] P. W. Anderson, “Ground state of a magnetic impurity in a metal,” *Phys. Rev.* **164**, 352–359 (1967).
- [81] R. I. Epstein, “Acoustic properties of neutron stars,” *The Astrophysical Journal* **333**, 880–894 (1988).
- [82] A. D. Sedrakian, “Neutron-phonon interaction in neutron stars: Phonon spectrum of Coulomb lattice,” *Astrophys. Space Sci.* **236**, 267–276 (1996).
- [83] P. Magierski, “In-medium ion mass renormalization and lattice vibrations in the neutron star crust,” *Int. J. Mod. Phys. E* **13**, 371–374 (2004).
- [84] P. Magierski and A. Bulgac, “Nuclear hydrodynamics in the inner crust of neutron stars,” *Acta Phys. Pol. B* **35**, 1203 (2004).
- [85] N. Martin and M. Urban, “Superfluid hydrodynamics in the inner crust of neutron stars,” *Phys. Rev. C* **94**, 065801 (2016).
- [86] N. Chamel, D. Page and S. Reddy, “Low-energy collective excitations in the neutron star inner crust,” *Phys. Rev. C* **87**, 035803 (2013).
- [87] K. Sekizawa, S. Kobayashi and M. Matsuo, “Time-dependent extension of the self-consistent band theory

- for neutron star matter: Anti-entrainment effects in the slab phase,” *Phys. Rev. C* **105**, 045807 (2022).
- [88] K. Yoshimura and K. Sekizawa, “Superfluid extension of the self-consistent time-dependent band theory for neutron star matter: Anti-entrainment vs. superfluid effects in the slab phase,” arXiv preprint arXiv:2306.03327 (2023).
- [89] N. N. Shchepochin, N. Chamel and J. M. Pearson, “Unified equations of state for cold nonaccreting neutron stars with Brussels-Montreal functionals. IV. Role of the symmetry energy in pasta phases,” *Phys. Rev. C* **108**, 025805 (2023).
- [90] Daniel Pęczak, Agata Zdanowicz, Nicolas Chamel, Piotr Magierski, and Gabriel Wlazłowski, “Dataset and supplement for "Time-dependent nuclear energy-density functional theory toolkit for neutron star crust: dynamics of a nucleus in a neutron superfluid",” (2024).
- [91] V. Allard and N. Chamel, “Gapless superfluidity in neutron stars: Thermal properties,” *Phys. Rev. C* **108**, 015801 (2023).
- [92] V. Allard and N. Chamel, “Gapless superfluidity in neutron stars: Normal-fluid fraction,” *Phys. Rev. C* **108**, 045801 (2023).
- [93] H. Dinh Thi, A.-F. Fantina and F. Gulminelli, “The proto-neutron star inner crust in the liquid phase,” *A&A* **672**, A160 (2023).
- [94] B. Carter, N. Chamel and P. Haensel, “Entrainment Coefficient and Effective Mass for Conduction Neutrons in Neutron Star Crust: Macroscopic Treatment,” *Int. J. Mod. Phys. D* **15**, 777–803 (2006).
- [95] C. Brandon, N. Chamel and P. Haensel, “Entrainment coefficient and effective mass for conduction neutrons in neutron star crust: simple microscopic models,” *Nucl. Phys. A* **748**, 675–697 (2005).
- [96] N. Chamel, “Band structure effects for dripped neutrons in neutron star crust,” *Nucl. Phys. A* **747**, 109–128 (2005).
- [97] N. Chamel, “Crustal Entrainment and Pulsar Glitches,” *Phys. Rev. Lett.* **110**, 011101 (2013).
- [98] J. Bardeen, “Critical Fields and Currents in Superconductors,” *Rev. Mod. Phys.* **34**, 667–681 (1962).
- [99] G. W. Rayfield and F. Reif, “Quantized vortex rings in superfluid helium,” *Phys. Rev.* **136**, A1194–A1208 (1964).
- [100] R. J. Donnelly, “Quantized vortices and turbulence in helium II,” *Annu. Rev. Fluid Mech.* **25**, 325–371 (1993).
- [101] W. J. Kwon, G. Moon, S. W. Seo and Y. Shin, “Critical velocity for vortex shedding in a Bose-Einstein condensate,” *Phys. Rev. A* **91**, 053615 (2015).
- [102] J. W. Park, B. Ko, Bumsuk and Y. Shin, “Critical vortex shedding in a strongly interacting fermionic superfluid,” *Phys. Rev. Lett.* **121**, 225301 (2018).
- [103] T. Winiecki and C. S. Adams, “Motion of an object through a quantum fluid,” *Europhys. Lett. (EPL)* **52**, 257–263 (2000).
- [104] T. Frisch, Y. Pomeau and S. Rica, “Transition to dissipation in a model of superflow,” *Phys. Rev. Lett.* **69**, 1644–1647 (1992).
- [105] K. Sasaki, N. Suzuki and H. Saito, “Bénard–von Kármán vortex street in a Bose-Einstein condensate,” *Phys. Rev. Lett.* **104**, 150404 (2010).
- [106] C. F. Barenghi and R. J. Donnelly, “Vortex rings in classical and quantum systems,” *Fluid Dyn. Res.* **41**, 051401 (2009).
- [107] S. Fujiyama, A. Mitani, M. Tsubota, D. I. Bradley, S. N. Fisher, A. M. Guénault, R. P. Haley, G. R. Pickett and V. Tsepelin, “Generation, evolution, and decay of pure quantum turbulence: A full biot-savart simulation,” *Phys. Rev. B* **81**, 180512 (2010).
- [108] S. Fujiyama and M. Tsubota, “Drag force on an oscillating object in quantum turbulence,” *Phys. Rev. B* **79**, 094513 (2009).
- [109] H. Adachi, S. Fujiyama and M. Tsubota, “Steady-state counterflow quantum turbulence: Simulation of vortex filaments using the full Biot-Savart law,” *Phys. Rev. B* **81**, 104511 (2010).
- [110] A. Nakatsuji, M. Tsubota and H. Yano, “Statistics of vortex loops emitted from quantum turbulence driven by an oscillating sphere,” *Phys. Rev. B* **89**, 174520 (2014).
- [111] D. Antonopoulou, B. Haskell and C. M. Espinoza, “Pulsar glitches: observations and physical interpretation,” *Rep. Prog. Phys.* **85**, 126901 (2022).
- [112] C. Peralta, A. Melatos, M. Giacobello, and A. Ooi, “Transitions between Turbulent and Laminar Superfluid Vorticity States in the Outer Core of a Neutron Star,” *Astrophys. J.* **651**, 1079–1091 (2006).
- [113] G. Wlazłowski, K. Sekizawa, P. Magierski, A. Bulgac and M. McNeil Forbes, “Vortex pinning and dynamics in the neutron star crust,” *Phys. Rev. Lett.* **117**, 232701 (2016).
- [114] A. Bulgac, M. McNeilForbes and R. Sharma, “Strength of the vortex-pinning interaction from real-time dynamics,” *Phys. Rev. Lett.* **110**, 241102 (2013).
- [115] N. Chamel and P. Haensel, “Physics of Neutron Star Crusts,” *Living Reviews in Relativity* **11**, 10 (2008).
- [116] V. Graber, N. Andersson and M. Hogg, “Neutron stars in the laboratory,” *Int. J. Mod. Phys. D* **26**, 1730015 (2017).
- [117] G. Scamps, S. Goriely, E. Olsen, M. Bender and W. Ryssens, “Skyrme–Hartree–Fock–Bogoliubov mass models on a 3D mesh: effect of triaxial shape,” *Eur. Phys. J. A* **57** (2021), 10.1140/epja/s10050-021-00642-1.
- [118] W. Ryssens, G. Scamps, S. Goriely and M. Bender, “Skyrme–Hartree–Fock–Bogoliubov mass models on a 3D mesh: II. Time-reversal symmetry breaking,” *Eur. Phys. J. A* **58** (2022), 10.1140/epja/s10050-022-00894-5.
- [119] W. Ryssens, G. Scamps, S. Goriely and M. Bender, “Skyrme–Hartree–Fock–Bogoliubov mass models on a 3D mesh: IIb. Fission properties of BSkG2,” *Eur. Phys. J. A* **59** (2023), 10.1140/epja/s10050-023-01002-x.
- [120] G. Grams, W. Ryssens, G. Scamps, S. Goriely and N. Chamel, “Skyrme–Hartree–Fock–Bogoliubov mass models on a 3D mesh: III. From atomic nuclei to neutron stars,” (2023), arXiv:2307.14276 [nucl-th].
- [121] A. Pastore, M. Martini, D. Davesne, J. Navarro, S. Goriely and N. Chamel, “Linear response theory and neutrino mean free path using Brussels-Montreal Skyrme functionals,” *Phys. Rev. C* **90**, 025804 (2014).
- [122] J. S. Levinger, *Nuclear Photo-Disintegration* (Oxford University Press, Oxford, 1960).
- [123] M. N. Harakeh and A. van der Woude, *Giant Resonances* (Oxford University Press, Oxford, 2001).
- [124] G. F. Bertsch, P. F. Bortignon and R. A. Broglia, “Damping of nuclear excitations,” *Rev. Mod. Phys.* **55**, 287–314 (1983).

- [125] P. Ring and P. Schuck, *The nuclear many-body problem* (Springer Science & Business Media, 2004).

**Supplementary Material for:
Time-dependent nuclear energy-density functional theory toolkit
for neutron star crust dynamics: quantifying effective mass**

Daniel Pećak,^{1,2,*} Agata Zdanowicz,¹ Nicolas Chamel,^{3,†} Piotr Magierski,^{1,4,‡} and Gabriel Wlazłowski^{1,4,§}

¹*Faculty of Physics, Warsaw University of Technology, Ulica Koszykowa 75, 00-662 Warsaw, Poland*

²*Institute of Physics, Polish Academy of Sciences, Aleja Lotników 32/46, PL-02668 Warsaw, Poland*

³*Institut d'Astronomie et d'Astrophysique, CP-226, Université Libre de Bruxelles, 1050 Brussels, Belgium*

⁴*Department of Physics, University of Washington, Seattle, WA 981951560, USA*

(Dated: February 26, 2024)

In this Supplementary Material, we provide a list of accompanying movies.

The table below provides the list of accompanying movies, with information about applied external force F and density of the inner crust $\bar{\rho}$. We have selected only these cases where quantum vortices are nucleated.

$\bar{\rho}$ [fm ⁻³]	F [MeV/fm]	file name	YouTube link
0.0023	0.5	n0.002F0.5r1.mp4	https://youtu.be/Pa0M3R9bJww
0.0023	1.0	n0.002F1.0r1.mp4	https://youtu.be/ocR_177S_Cc
0.0058	0.5	n0.006F0.5r1.mp4	https://youtu.be/TVKxAqJ-r50
0.0058	1.0	n0.006F1.0r1.mp4	https://youtu.be/wsGtvhutXGs
0.0058	2.0	n0.006F2.0r1.mp4	https://youtu.be/GS0yziDBZ68
0.0104	1.0	n0.010F1.0r1.mp4	https://youtu.be/8yw_k4nyn9k
0.0104	2.0	n0.010F2.0r1.mp4	https://youtu.be/nlANRhzhVp8
0.0148	2.0	n0.015F2.0r1.mp4	https://youtu.be/pu3LfHhtqvU

* daniel.pecak@pw.edu.pl

† nicolas.chamel@ulb.be

‡ piotrm@uw.edu

§ gabriel.wlazlowski@pw.edu.pl